

# Stable stratification promotes multiple zonal jets in a turbulent Jovian dynamo model

T. Gastine<sup>a</sup>, J. Wicht<sup>b,\*</sup>

<sup>a</sup>Université de Paris, Institut de Physique du Globe de Paris, UMR 7154 CNRS, 1 rue Jussieu, F-75005, Paris, France

<sup>b</sup>Max Planck Institut für Sonnensystemforschung, Justus-von-Liebig-Weg 3, 37077, Göttingen, Germany

## ARTICLE INFO

### Keywords:

Jupiter interior  
Atmospheres dynamics  
Magnetohydrodynamics (MHD)  
Numerical simulations

## ABSTRACT

The ongoing NASA's Juno mission puts new constraints on the internal dynamics of Jupiter. Data gathered by its onboard magnetometer reveal a dipole-dominated surface magnetic field accompanied by strong localised magnetic flux patches. The gravity measurements indicate that the fierce surface zonal jets extend several thousands of kilometers below the cloud level before rapidly decaying below  $0.94 - 0.96 R_J$ ,  $R_J$  being the mean Jovian radius at the one bar level. Jupiter's internal structure can be grossly decomposed in two parts: (i) an outer layer filled with a mixture of molecular hydrogen and helium where the zonal flows are thought to be driven; (ii) an inner region where hydrogen becomes metallic and dynamo action is expected to sustain the magnetic field. Several internal models however suggest a more intricate structure with a thin intermediate region in which helium would segregate from hydrogen, forming a compositionally-stratified layer. Here, we develop the first global Jovian dynamo which incorporates an intermediate stably-stratified layer between  $0.82 R_J$  and  $0.86 R_J$ . Using much lower diffusivities than previous models enables us to more clearly separate the dynamics of the metallic core and the molecular envelope. Analysing the energy balance reveals that the magnetic energy is almost one order of magnitude larger than kinetic energy in the metallic region, while most of the kinetic energy is pumped into zonal motions in the molecular envelope. Those result from the different underlying force hierarchy with a triple balance between Lorentz, Archimedean and ageostrophic Coriolis forces in the metallic core and inertia, buoyancy and ageostrophic Coriolis forces controlling the external layers. The simulation presented here is the first to demonstrate that multiple zonal jets and dipole-dominated dynamo action can be consolidated in a global simulation. The inclusion of a stable layer is a necessary ingredient that allows zonal jets to develop in the outer envelope without contributing to the dynamo action in the deeper metallic region. Stable stratification however also smooths out the small-scale features of the magnetic field by skin effect, yielding a too-dipolar surface field as compared to the observations. These constraints suggest that possible stable layers in Jupiter should be located much closer to the surface ( $0.9 - 0.95 R_J$ ).

## 1. Introduction

The banded structures observed at Jupiter's surface correlate with strong prograde (or eastward) and retrograde (or westward) winds. A strong prograde equatorial jet reaching 150 m/s extends over  $\pm 15^\circ$  latitude. It is flanked by alternating jets with weaker amplitudes around 10–20 m/s up to the polar regions. The depth to which those winds penetrate into Jupiter has been debated intensely over the last decades (for a review, see Vasavada and Showman, 2005). In the “weather layer” scenario, the zonal jets are confined to a thin layer close to the cloud levels (e.g. Cho and Polvani, 1996; Lian and Showman, 2010), while under the “deep convection” hypothesis the zonal winds could penetrate deep over  $10^3$  to  $10^4$  km (e.g. Busse, 1976; Christensen, 2002; Heimpel, Aurnou and Wicht, 2005; Jones and Kuzanyan, 2009). Those two end-member scenarios also differ in the nature of the physical mechanism responsible for sustaining the jets. Possible candidates range from shallow moist convection at the cloud level to deep convective motions in Jupiter's interior. For both physical forcings, rapid rotation is instrumental for providing a statistical correlation that allows feeding energy from small scale convection in the larger scale jets (Rhines,

1975). Because of rapid rotation and the associated Taylor-Proudman theorem, the jets could penetrate deep into the molecular envelope even when they are only driven in a shallow weather layer (Showman, Gierasch and Lian, 2006).

Determining the actual depth of the Jovian zonal jets is one of the main goals of the ongoing NASA Juno mission (Bolton, Lunine, Stevenson, Connerney, Levin, Owen, Bagenal, Gautier, Ingersoll, Orton, Guillot, Hubbard, Bloxham, Coradini, Stephens, Mokashi, Thorne and Thorpe, 2017). Using Juno's gravity measurements (Iess, Folkner, Durante, Parisi, Kaspi, Galanti, Guillot, Hubbard, Stevenson, Anderson, Buccino, Casajus, Milani, Park, Racioppa, Serra, Tortora, Zannoni, Cao, Helled, Lunine, Miguel, Militzer, Wahl, Connerney, Levin and Bolton, 2018), Kaspi, Galanti, Hubbard, Stevenson, Bolton, Iess, Guillot, Bloxham, Connerney, Cao, Durante, Folkner, Helled, Ingersoll, Levin, Lunine, Miguel, Militzer, Parisi and Wahl (2018) infer that the equatorially-antisymmetric component of the zonal jets are reduced to an amplitude of 1% of their surface values 3000 km below the one bar level. However, the interpretation of gravity perturbations in terms of zonal flows is complicated and other zonal flow profiles could be envisioned (e.g. Kong, Zhang, Schubert and Anderson, 2018; Wicht, Dietrich, Wulff and Christensen, 2020; Galanti and Kaspi, 2021).

\*Corresponding author. E-mail: gastine@ipgp.fr

ORCID(s): 0000-0003-4438-7203 (T. Gastine); 0000-0002-2440-5091 (J. Wicht)

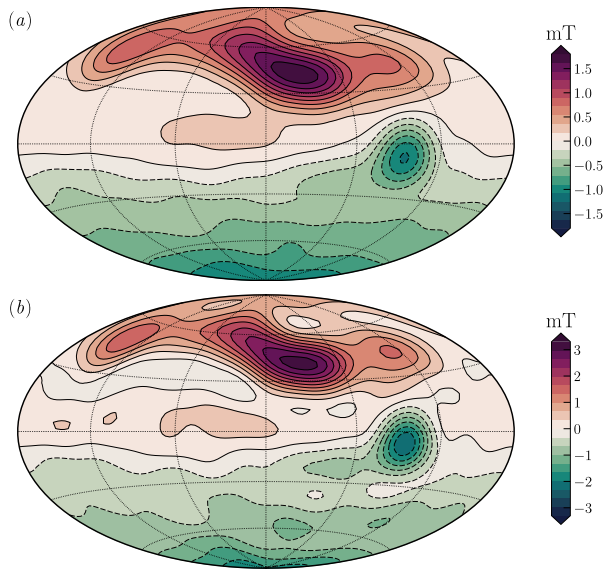


**Figure 1:** Hammer projections of the radial component of the magnetic field at the surface of Jupiter (upper panel) and at  $0.9 R_J$  (lower panel). These maps have been reconstructed using the JRM09 Jovian field model by Connerney et al. (2018).

Several additional arguments favour comparable depths of 3000 to 4000 km. A first indication comes from studies of rapidly-rotating convection in thin spherical shells. Such numerical models have been developed to focus on the dynamics of the molecular envelope of the gas giants. They succeed in reproducing several key features of the observed zonal flow pattern such as a dominant prograde equatorial jet (e.g. Christensen, 2002), multiple jets of alternated directions (Heimpel et al., 2005; Jones and Kuzanyan, 2009; Gastine, Heimpel and Wicht, 2014a), or the formation of large scale vortices (Heimpel, Gastine and Wicht, 2016). The width of the main prograde equatorial jet directly depends on the thickness of the simulated spherical shell (e.g. Heimpel and Aurnou, 2007). Best agreement with Jupiter is obtained when the lower boundary is set to  $0.95 R_J$ .

Another set of constraints on the zonal winds depth comes from the Jovian magnetic field. Using Juno's first nine orbits, Connerney et al. (2018) have constructed the JRM09 internal field model up to the harmonic degree  $\ell = 10$  shown in Fig. 1. The surface field (upper panel) is dominated by a tilted dipole and features intense localised flux concentrations. The downward continuation of the surface field to  $0.9 R_J$  (Fig. 1b) reveals an intricate field morphology with clear differences between the northern and southern hemispheres. In the northern hemisphere, the field is strongly concentrated in a latitudinal band, while the southern hemisphere is dominated by a pronounced field concentration just below the equator (Moore, Yadav, Kulowski, Cao, Bloxham, Connerney, Kotsiaros, Jørgensen, Merayo, Stevenson, Bolton and Levin, 2018).

A comparison of Juno's measurements with magnetic data from previous space missions, such as Pioneer or Voyager, shows only mild changes over a time span of 45 years

(Ridley and Holme, 2016; Moore, Cao, Bloxham, Stevenson, Connerney and Bolton, 2019). This suggests an upper bound for the jet speed of roughly 1 cm/s at a depth where magnetic effects start to matter at about  $0.94 R_J$ .

Different lines of arguments therefore suggest a lower boundary for the jets located around  $0.94 - 0.96 R_J$ . Which mechanism could possibly quench the jets in this depth range? Two alternatives have been suggested so far: Lorentz forces or a stably stratified layer.

Lorentz forces rely on electric currents and thus depend on the electrical conductivity. Experimental data (e.g. Weir, Mitchell and Nellis, 1996; Nellis, Weir and Mitchell, 1999; Knudson, Desjarlais, Preising and Redmer, 2018) and *ab initio* simulations (see French, Becker, Lorenzen, Nettelmann, Bethkenhagen, Wicht and Redmer, 2012; Knudson et al., 2018, and references therein) indicate that the electrical conductivity increases at a super-exponential rate with depth due to the ionization of molecular hydrogen. At pressures of about one Mbar, however, hydrogen assumes a metallic state and the conductivity increases much more mildly. Here we use a model based on the *ab initio* simulations by French et al. (2012), which puts the transition to metallic hydrogen at about  $0.9 R_J$ . However, many aspects of the conductivity profile remain debated. This includes the depth of the phase transition and the question of whether it is a first order or a gradual second order transition (for a review see Stevenson, 2020).

A key parameter for estimating dynamo action is the magnetic Reynolds number  $Rm$  which quantifies the ratio of induction and magnetic diffusion. In the outer envelope where the electrical conductivity increases extremely steeply, Liu, Goldreich and Stevenson (2008) showed that  $Rm = U_z d_\sigma \sigma \mu_0$  provides a more appropriate definition of the magnetic Reynolds number associated with zonal motions (see also Cao and Stevenson, 2017). Here  $U_z$  is the typical zonal flow velocity,  $\mu_0$  the vacuum permeability and  $d_\sigma = |\partial \ln \sigma / \partial r|^{-1}$  the electrical conductivity scale height. As long as  $Rm$  remains smaller than unity, the zonal flows merely modify the field that is produced in the deeper interior (Wicht, Gastine and Duarte, 2019a). In Jupiter, this region extends down to about  $0.96 R_J$  (Wicht, Gastine, Duarte and Dietrich, 2019b). Lorentz forces then simply scale with  $\sigma$  (Wicht et al., 2019a) and thus remain negligible in the very outer region but kick in abruptly at a certain depth.

While this suggests that Lorentz forces are a good candidate for quenching the jets, several numerical simulations reveal a different picture. Instead of producing multiple alternating jets as the non-magnetic models, global dynamo simulations that adopt Jupiter's electrical conductivity profile only feature one main prograde equatorial jet aligned with the rotation axis, that mostly resides in the outer weakly conducting region. Strong azimuthal Lorentz forces in the metallic interior suppress zonal motions along the axis of rotation and kill or significantly brake all other jets (Heimpel and Gómez Pérez, 2011; Duarte, Gastine and Wicht, 2013; Jones, 2014; Gastine, Wicht, Duarte, Heimpel and Becker,

2014b; Dietrich and Jones, 2018; Duarte, Wicht and Gastine, 2018). Instead of explaining the observed depth, Lorentz forces seem to yield an unrealistic jet amplitude and structure (Christensen, Wicht and Dietrich, 2020).

Another candidate that could prevent jets from penetrating deeper is a stably stratified layer that would inhibit the convective mixing. The Juno gravity observations suggest that Jupiter consists of several distinct layers: (i) an outer envelope with reduced He (and Ne) abundance compared to the primordial solar value, (ii) an intermediate envelope with a higher He abundance and possibly a lower abundance of heavier elements, (iii) a deeper interior sometimes called a diluted core with an increased heavier element abundance, and (iv) possibly a denser core (Wahl, Hubbard, Militzer, Guillot, Miguel, Movshovitz, Kaspi, Helled, Reese, Galanti, Levin, Connerney and Bolton, 2017; Debras and Chabrier, 2019; Stevenson, 2020).

Stable stratification could help to explain how the different layers formed and were preserved over time. In gas giant planets, such stable layers could possibly occur when helium segregates from hydrogen due to its poor miscibility (e.g. Stevenson, 1980; Lorenzen, Holst and Redmer, 2011). Below a critical temperature, helium tends to separate from hydrogen and forms droplets that rain towards the interior. This leads to helium depletion of the outer envelope and leaves a helium stably-stratifying gradient that separates the outer envelope from the interior. However, it remains unclear whether this process has already started in Jupiter (Militzer, Soubiran, Wahl and Hubbard, 2016; Schöttler and Redmer, 2018). If so, estimates put the upper boundary of the related stable layer around 1 Mbar, which roughly corresponds to  $0.9 R_J$ . The recent interior models by Debras and Chabrier (2019) put the upper boundary of the stable layer at  $0.93 R_J$  and the lower bound somewhere between  $0.8 R_J$  and  $0.9 R_J$ .

In the limit of rapid rotation, the dynamical influence of a stably-stratified layer (hereafter SSL) depends on the ratio of the Brunt-Väisälä frequency  $N$  to the rotation rate  $\Omega$ . Using a linear model of non-magnetic rotating convection, Takehiro and Lister (2001) have shown that the distance of penetration  $\delta$  of a convective feature of size  $d_c$  into a stratified layer follows  $\delta \sim (N/\Omega)^{-1} d_c$ . Numerical models by Gastine, Aubert and Fournier (2020) showed that this scaling still holds in nonlinear dynamo models. The penetration of zonal flows into such layers is more intricate since it directly depends on the thermal structure at the edge of the SSL (e.g. Showman et al., 2006). The global numerical models of solar-type stars by Brun, Strugarek, Varela, Matt, Augustson, Emeriau, DoCao, Brown and Toomre (2017) show that the zonal motions do not penetrate into the stably-stratified interior when  $N/\Omega \gg 1$  (see also Browning, Brun and Toomre, 2004; Augustson, Brun and Toomre, 2016). This ratio, however, remains poorly known in Jupiter's interior. The internal models by Debras and Chabrier (2019) suggest  $1 \leq N/\Omega \leq 3$ . (Christensen et al., 2020). Considering simplified 2-D axisymmetric numerical models where the zonal flows are forced by an analytical source term, Christensen et al. (2020) claim that stable stratification alone is not

sufficient to brake the geostrophic zonal winds. They suggest that weak Lorentz forces drive a weak meridional flow that penetrate the upper edge of the SSL, encountering the strong stable stratification. This in turn alters the latitudinal entropy structure that explains the quenching of the jets according to the thermal wind balance.

Here we adopt the idea of a stably-stratified sandwich layer and, for the first time, study its impact on the zonal jets and overall dynamics in a full 3-D global dynamo simulation. The paper is organised as follows. Numerical model and methods are detailed in § 2. Section 3 is dedicated to the description of the results, while the implications for Jupiter are further discussed in § 4.

## 2. Model and methods

### 2.1. Defining a non-adiabatic reference state

We consider a magnetohydrodynamic simulation of a conducting fluid in a spherical shell of radius ratio  $r_i/r_o$  rotating at a constant rotation rate  $\Omega$  about the  $z$ -axis. We adopt the so-called ‘‘Lantz-Braginsky-Roberts’’ anelastic approximation of the Navier-Stokes equations introduced by Braginsky and Roberts (1995) and Lantz and Fan (1999). It allows the incorporation of the radial dependence of the background state while filtering out the fast acoustic waves that would otherwise significantly hamper the timestep size. Within the anelastic approximation, one actually solves for small perturbations around a background state that is frequently assumed to be well-mixed and adiabatic (e.g. Jones, Boronski, Brun, Glatzmaier, Gastine, Miesch and Wicht, 2011; Verhoeven, Wiesehöfer and Stellmach, 2015).

Here we follow a slightly different approach. Since we aim at modelling the effects of a stably stratified layer at the top of the metallic region, we define a reference state that can depart from the adiabat. This is a common approach in solar convection models that incorporate both the radiative core and the convective envelope (e.g. Alvan, Brun and Mathis, 2014). Practically, this implies that any physical quantity  $x$  is expanded in spherical coordinates  $(r, \theta, \phi)$  as follows

$$x(r, \theta, \phi, t) = \tilde{x}(r) + x'(r, \theta, \phi, t), \quad (1)$$

where the tilde denotes the spherically-symmetric and static background state, while the primes correspond to fluctuations about this mean. To ensure the validity of the anelastic approximation when using a non-adiabatic reference state, the perturbations should remain small as compared to the background state (e.g. Gough, 1969), i.e.

$$\frac{|x'|}{|x|} \ll 1, \quad \forall(r, \theta, \phi, t).$$

In the following, we adopt a dimensionless formulation of the MHD equations. Starting with the background reference state, the physical quantities such as the background density  $\bar{\rho}$ , temperature  $\bar{T}$ , gravity  $\bar{g}$  and entropy gradient  $d\bar{s}/dr$  are non-dimensionalised with respect to their value at the outer

radius  $r_o$ . We adopt the spherical shell gap  $d = r_o - r_i$  as the reference lengthscale.

To precisely control the location and the degree of stratification of the SSL, a possible approach consists in prescribing the functional form of the background entropy gradient  $d\tilde{s}/dr$  (see for instance Takehiro and Lister, 2001; Gastine et al., 2020, for geodynamo models). Regions with a negative gradient  $d\tilde{s}/dr < 0$  are super-adiabatic and hence prone to harbour convective motions, while the fluid layers with  $d\tilde{s}/dr > 0$  are stably stratified. In the following, we assume a constant degree of stratification  $d\tilde{s}/dr = \Gamma_s$  between the radii  $\mathcal{R}_i$  and  $\mathcal{R}_o$  and a constant dimensionless negative gradient  $d\tilde{s}/dr = -1$  in the surrounding convective layers. Those regions are then smoothly connected with tanh functions centered at  $\mathcal{R}_i$  and  $\mathcal{R}_o$ :

$$\frac{d\tilde{s}}{dr} = \frac{1 + \Gamma_s}{4} \left[ 1 + f_{\mathcal{R}_i}(r) \right] \left[ 1 - f_{\mathcal{R}_o}(r) \right] - 1, \quad (2)$$

where

$$f_a(r) = \tanh[\zeta_s(r - a)], \quad \mathcal{R}_o = \mathcal{R}_i + H_s,$$

$H_s$  is the thickness of the stably stratified layer and  $\zeta_s$  the stiffness of the transition. As we will see below, the degree of stratification  $\Gamma_s$  can be directly related to the value of the Brunt-Väisälä frequency of the stably-stratified layer. Figure 2 shows the radial profile of  $d\tilde{s}/dr$  employed in this study. It features a stably-stratified layer between the radii  $\mathcal{R}_i = 0.84r_o$  and  $\mathcal{R}_o = 0.88r_o$ , which correspond to  $H_s = 0.05$ . The degree of stratification is set to  $\Gamma_s = 2000$ , while the stiffness of the transition is  $\zeta_s = 200$ . The location and thickness of the SSL have been chosen according to the internal models by Militzer et al. (2016) and Wahl et al. (2017). Because of the finite size of the transitions,  $d\tilde{s}/dr$  changes sign before (after)  $\mathcal{R}_i$  ( $\mathcal{R}_o$ ), yielding a stably-stratified layer with an effective thickness larger than  $H_s$ . Imposing a background entropy gradient coming from stellar evolution models is commonly used in simulations of stellar interior dynamics (e.g. Browning et al., 2004; Augustson et al., 2016; Brun et al., 2017) for introducing a stably-stratified region. In absence of a more realistic entropy profile coming from internal models of Jupiter, we adopt here a parametrized background entropy gradient. While being convenient, it lacks a proper physical justification and simply maintains the stratification by introducing an effective entropy or heat sink. A more realistic distribution of entropy or heat sources in the convective layer of Jupiter is discussed by Jones (2014).

Once the background entropy gradient has been specified, the reference temperature and density gradients can be expressed via the following thermodynamic relations

$$\frac{d \ln \tilde{T}}{dr} = \epsilon_s \frac{d\tilde{s}}{dr} - Di \tilde{\alpha} \tilde{g}, \quad (3)$$

and

$$\frac{d \ln \tilde{\rho}}{dr} = -Co \epsilon_s \tilde{\alpha} \tilde{T} \frac{d\tilde{s}}{dr} - \frac{Di}{\Gamma_o} \frac{\tilde{\alpha} \tilde{g}}{\tilde{\Gamma}}, \quad (4)$$

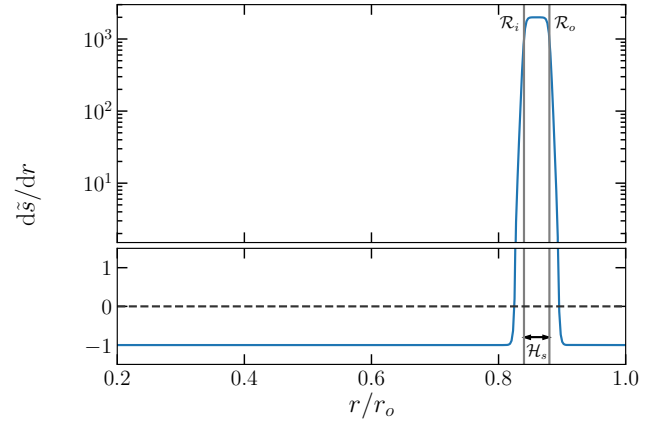


**Figure 2:** Background entropy gradient  $d\tilde{s}/dr$  as a function of the normalised radius  $r/r_o$  as defined by Eq. (2) with  $H_s = 0.05$ ,  $\Gamma_s = 2000$ ,  $\mathcal{R}_i/r_o = 0.84$ ,  $\mathcal{R}_o/r_o = 0.88$  and  $\zeta_s = 200$ . The two vertical solid lines mark the boundaries of the SSL  $\mathcal{R}_i$  and  $\mathcal{R}_o$ . The horizontal dashed line corresponds to the neutral stratification  $d\tilde{s}/dr = 0$ , which delineates the separation between super adiabatic and stable stratification. To highlight the values of the profile in the convective regions, the y axis has been split into logarithmic scale when  $d\tilde{s}/dr > 1.5$  (upper panel) and linear scale for the values between  $-1.5$  and  $1.5$  (lower panel).

where  $\tilde{\alpha}$  denotes the dimensionless expansion coefficient, while  $\tilde{\Gamma}$  is the Grüneisen parameter normalised by its value at  $r_o$ . The equations (3-4) involve four dimensionless parameters

$$Di = \frac{\alpha_o g_o d}{c_p}, \quad Co = \alpha_o T_o, \quad \Gamma_o, \quad \epsilon_s = \frac{d}{c_p} \left| \frac{d\tilde{s}}{dr} \right|_{r_o}. \quad (5)$$

According to the *ab initio* calculations by French et al. (2012), the heat capacity  $c_p$  exhibits little variation in most of Jupiter's interior and is hence assumed to be constant in the above equations.  $Di$  denotes the dissipation number, which characterises the ratio between the fluid layer thickness and the temperature scale,  $Di = d/d_T$  with  $d_T = c_p/\alpha_o g_o$ . In the so-called *thin-layer limit* of  $d \ll d_T$ ,  $Di$  vanishes and yields the Boussinesq approximation of the Navier-Stokes equations (e.g. Verhoeven et al., 2015).  $Co$  is the compressibility number that is equal to unity when the fluid is an ideal gas, and is  $\mathcal{O}(10^{-2})$  in liquid iron cores of terrestrial planets (see Anufriev, Jones and Soward, 2005). In the above equations,  $\Gamma_o$  corresponds to the Grüneisen parameter at the outer boundary, while  $\epsilon_s$  characterises the departure of the background state from the adiabat. It has to satisfy  $\epsilon_s \ll 1$  to ensure the consistency of the anelastic approximation (Gilman and Glatzmaier, 1981). In standard anelastic models such as the ones employed in the benchmarks by Jones et al. (2011), the background state is assumed to be a perfectly adiabatic ideal gas (i.e.  $\epsilon_s = 0$ ,  $Co = 1$ ). The background state is in this case entirely specified by two parameters only:  $Di$  and  $\Gamma_o$ ,  $Di$  being directly related to the number of density scale heights of the reference state (see Jones and Kuzanyan,

2009, their Eq. 2.9), and  $\Gamma_o$  is the inverse of the polytropic index.

At this stage, given that  $\tilde{\alpha}$  and  $\tilde{\Gamma}$  directly depend on  $\tilde{\rho}$  and  $\tilde{T}$ , the equations (3-4) coupled with the additional Poisson equation for gravity form a nonlinear problem that would necessitate an iterative solver (for an example, see e.g. Brun, Miesch and Toomre, 2011). For the sake of simplicity and to ensure the future reproducibility of our results, we adopt here a grosser approach which consists of approximating  $\tilde{\alpha}$ ,  $\tilde{g}$  and  $\tilde{\Gamma}$  by analytical functions which fit the interior model of French et al. (2012). The A enlists the numerical values of the approximated profiles of  $\tilde{g}$ ,  $\tilde{\alpha}$  and  $\tilde{\Gamma}$ . A comparable approach was followed by Jones (2014) to define the reference state of his Jupiter dynamo models.

Figure 3 shows a comparison between the reference state considered in this study using  $Di = 28.417$ ,  $Co = 0.73$  and  $\Gamma_o = 0.4$  (solid lines) with the *ab initio* models from French et al. (2012) (dashed lines). Most of the density and temperature contrasts are accommodated in the external 10% of Jupiter's interior. Global models of rotating convection in anelastic spherical shells indicate that a steeply-decreasing background density goes along with smaller convective flow lengthscales (e.g. Gastine and Wicht, 2012, their Fig. 5). Resolving the entire density contrast up to the 1 bar level would yield a lengthscale range that would become numerically prohibitive. As shown in Fig. 3, we hence restrain the numerical fluid domain to an interval that spans  $0.196 R_J$  to  $0.98 R_J$ , with  $r_i/r_o = 0.2$ . Except explicitly-stated otherwise, the conversion between dimensionless and dimensional units is done by simple multiplication with the reference values at  $r_o = 0.98 R_J$  given in Tab. 1.

Though not fully thermodynamically consistent, the approximated reference state hence provides background profiles in good agreement with the interior models while keeping the reference state definition tractable.

## 2.2. Transport properties

The *ab initio* calculations by French et al. (2012) suggest that the kinematic viscosity is almost homogeneous in Jupiter's interior with values around  $\nu \simeq 3 \times 10^{-7}$  m<sup>2</sup>/s (see Tab. 1). In the following, we therefore simply adopt a constant kinematic viscosity. The thermal diffusivity exhibits a more complex variation. It gradually decreases outward up to  $0.9 R_J$ , above which it increases due to additional ionic transport becoming relevant there. The overall variations are, however, limited to a factor of roughly 30. Following our previous models (Gastine et al., 2014b), we neglect those variations and assume a constant thermal diffusivity  $\kappa$  for simplicity. The electrical conductivity exhibits much steeper variations. A very abrupt increase inwards of the conductivity in the molecular envelope transitions around  $0.9 R_J$  to shallower variations in the metallic core. This profile is approximated in the numerical models by the continuous

functions introduced by Gómez-Pérez, Heimpel and Wicht (2010)

$$\tilde{\lambda} = \frac{1}{\tilde{\sigma}}, \quad \tilde{\sigma} = \begin{cases} 1 + (\tilde{\sigma}_m - 1) \left( \frac{r - r_i}{\mathcal{H}_m} \right)^{\xi_m}, & r \leq r_m, \\ \tilde{\sigma}_m \exp \left( \xi_m \frac{r - r_m}{\mathcal{H}_m} \frac{\tilde{\sigma}_m - 1}{\tilde{\sigma}_m} \right), & r \geq r_m, \end{cases} \quad (6)$$

where  $r_m$  is the radius that separates the two functions,  $\tilde{\sigma}_m$  denotes the dimensionless conductivity at  $r_m$ ,  $\xi_m$  the rate of the exponential decay and  $\mathcal{H}_m = r_m - r_i$  is the thickness of the metallic region. Given the abrupt decay of electrical conductivity in the outer layer, we choose the value at the inner boundary  $r_i$  for defining the reference magnetic diffusivity, in contrast with the other internal properties. Figure 3f shows a comparison between the electrical conductivity profile from French et al. (2012) and Eq. (6) with the parameters  $r_m = 0.9 r_o$ ,  $\tilde{\sigma}_m = 0.07$  and  $\xi_m = 11$  adopted in this study. The main difference between the two profiles arises in the metallic interior where we assume a constant electrical conductivity, while the *ab initio* calculations suggest a linear increase with depth. While  $Rm$  is limited to a few thousands in global models, it is expected to reach  $\mathcal{O}(10^5 - 10^6)$  in Jupiter's interior (e.g. Yadav et al., 2013). We hence anticipate that the linear decrease of conductivity would have a much stronger dynamical impact at the moderate values of  $Rm$  accessible to numerical dynamos than in Jupiter. Assuming a constant electrical conductivity in the lower layer at least guarantees that  $Rm$  stays at a high level in this region. To ensure that no spurious currents develop when the conductivity becomes too low at the external boundary, we assume that the electrical currents actually vanish when  $\tilde{\sigma} < 10^{-5}$ , i.e. when  $r \geq 0.94 r_o$  (see Elstner, Meinel and Rüdiger, 1990; Dietrich and Jones, 2018).

## 2.3. MHD equations

Now that the spherically-symmetric and static background state and material properties have been specified, we consider the set of equations that govern the time evolution of the velocity  $\mathbf{u}$ , the magnetic field  $\mathbf{B}$  and the entropy fluctuation  $s'$ . The equations are non-dimensionalised using the viscous diffusion time  $d^2/\nu$  as the reference time scale,  $\nu/d$  as the velocity unit and  $\sqrt{\Omega\mu_0\lambda_i\rho_o}$  as the reference scale for the magnetic field. The entropy fluctuations  $s'$  are non-dimensionalised using the same unit as for  $\tilde{s}$ , i.e.  $d|ds/dr|_{r_o}$ . This yields the following set of non-dimensional equations

$$\nabla \cdot (\tilde{\rho}\mathbf{u}) = 0, \quad \nabla \cdot \mathbf{B} = 0, \quad (7)$$

$$\frac{D\mathbf{u}}{Dt} + \frac{2}{E} \mathbf{e}_z \times \mathbf{u} = -\nabla \left( \frac{p'}{\tilde{\rho}} \right) + \frac{1}{EPm\tilde{\rho}} \mathbf{j} \times \mathbf{B} - \frac{Ra}{Pr} \tilde{\alpha} \tilde{T} \mathbf{g} s' + \frac{1}{\tilde{\rho}} \nabla \cdot \mathbf{S}, \quad (8)$$

**Table 1**

Estimates of the physical properties of Jupiter's interior at two different depths. The material properties come from the *ab initio* calculations from French et al. (2012). The magnetic field amplitude at  $0.98 R_J$  comes from Connerney et al. (2018), while the velocity and magnetic field estimates at depth come from the anelastic scaling laws by Yadav, Gastine, Christensen and Duarte (2013) and Gastine et al. (2014b).

Quantity	Notation	Value	
Radius	$R_J$	$6.989 \times 10^7$ m	
Lengthscale	$d = 0.8 \times 0.98 \times R_J$	$5.479 \times 10^7$ m	
Rotation rate	$\Omega$	$1.75 \times 10^{-4}$ s $^{-1}$	
		Value at $0.196 R_J$	Value at $0.98 R_J$
Density	$\rho$	3990 kg/m $^3$	84.8 kg/m $^3$
Temperature	$T$	18000 K	2500 K
Gravity	$g$	18.1 m/s $^2$	27.2 m/s $^2$
Heat capacity	$c_p$	$1.36 \times 10^4$ J/kg/K	$1.29 \times 10^4$ J/kg/K
Thermal expansion	$\alpha$	$5.46 \times 10^{-6}$ K $^{-1}$	$2.58 \times 10^{-4}$ K $^{-1}$
Viscosity	$\nu$	$2.66 \times 10^{-7}$ m $^2$ /s	$3.92 \times 10^{-7}$ m $^2$ /s
Thermal diffusivity	$\kappa$	$2.70 \times 10^{-5}$ m $^2$ /s	$1.32 \times 10^{-6}$ m $^2$ /s
Electrical conductivity	$\sigma$	$3.05 \times 10^6$ S/m	$3.5 \times 10^{-4}$ S/m
Magnetic diffusivity	$\lambda$	0.261 m $^2$ /s	$2.3 \times 10^9$ m $^2$ /s
Convective velocity	$u_c$	$\mathcal{O}(10^{-2} - 10^{-1})$ m/s	1 m/s
Zonal velocity	$u_Z$	$\mathcal{O}(10^{-2} - 10^{-1})$ m/s	10 m/s
Magnetic field strength	$B$	$\mathcal{O}(10^{-2})$ T	$10^{-3}$ T

$$\frac{\partial \mathbf{B}}{\partial t} = \nabla \times \left( \mathbf{u} \times \mathbf{B} - \frac{\tilde{\lambda}}{Pm} \nabla \times \mathbf{B} \right), \quad (9)$$

and

$$\tilde{\rho} \tilde{T} \left( \frac{Ds'}{Dt} + u_r \frac{ds'}{dr} \right) = \frac{1}{Pr} \nabla \cdot (\tilde{\rho} \tilde{T} \nabla s') + \frac{Pr Di}{Ra} (\mathcal{Q}_\nu + \mathcal{Q}_\lambda), \quad (10)$$

where  $D/Dt = \partial/\partial t + \mathbf{u} \cdot \nabla$  corresponds to the substantial time derivative,  $p'$  is the pressure fluctuation,  $\mathbf{j} = \nabla \times \mathbf{B}$  is the current and  $\mathbf{S}$  is the traceless rate-of-strain tensor expressed by

$$S_{ij} = 2\tilde{\rho} \left( e_{ij} - \frac{1}{3} \frac{\partial u_i}{\partial x_j} \right), \quad e_{ij} = \frac{1}{2} \left( \frac{\partial u_i}{\partial x_j} + \frac{\partial u_j}{\partial x_i} \right). \quad (11)$$

In Eq. (10),  $\mathcal{Q}_\nu$  and  $\mathcal{Q}_\lambda$  correspond to the viscous and Ohmic heating terms defined by

$$\mathcal{Q}_\nu = 2\tilde{\rho} \left[ \sum_{i,j} e_{ij} e_{ji} - \frac{1}{3} (\nabla \cdot \mathbf{u})^2 \right], \quad \mathcal{Q}_\lambda = \frac{\tilde{\lambda}}{E Pm^2} \mathbf{j}^2. \quad (12)$$

Since global models cannot handle the small diffusivities of astrophysical bodies, we adopt here entropy diffusion as a primitive sub grid-scale model of thermal conduction (see Jones et al., 2011). This is a common approach in anelastic convective models (see Lantz and Fan, 1999) which becomes more questionable when modelling the transition to stably-stratified layers. Comparison of numerical models with temperature and entropy diffusion by Lecoanet, Brown, Zweibel,

Burns, Oishi and Vasil (2014) however yield quantitatively similar results. We hence adopt entropy diffusion throughout the entire fluid domain.

The set of equations (7-10) is controlled by four dimensionless numbers, namely the Rayleigh number  $Ra$ , the Ekman number  $E$ , the Prandtl number  $Pr$  and the magnetic Prandtl number  $Pm$

$$Ra = \frac{\alpha_o T_o g_o d^4}{c_p \nu \kappa} \left| \frac{ds}{dr} \right|_o, \quad E = \frac{\nu}{\Omega d^2}, \quad Pr = \frac{\nu}{\kappa}, \quad Pm = \frac{\nu}{\lambda_i}. \quad (13)$$

For rapidly-rotating fluids, a relevant measure of the degree of stratification is the ratio of the Brunt-Väisälä frequency to the rotation rate (Takehiro and Lister, 2001). This is related to the control parameter  $\Gamma_s$  via

$$\frac{N_m}{\Omega} = \max_r \sqrt{\tilde{\alpha}(r) \tilde{T}(r) \tilde{g}(r) \frac{Ra E^2}{Pr} \Gamma_s}. \quad (14)$$

## 2.4. Boundary conditions

We assume stress-free and impenetrable boundary conditions at both boundaries:

$$u_r = \frac{\partial}{\partial r} \left( \frac{u_\theta}{r} \right) = \frac{\partial}{\partial r} \left( \frac{u_\phi}{r} \right) = 0, \quad r = \{r_i, r_o\}. \quad (15)$$

Entropy is assumed to be fixed at the outer boundary, while the entropy gradient is imposed at the inner boundary:

$$\frac{\partial s'}{\partial r} \Big|_{r=r_i} = 0, \quad s'(r=r_o) = 0. \quad (16)$$

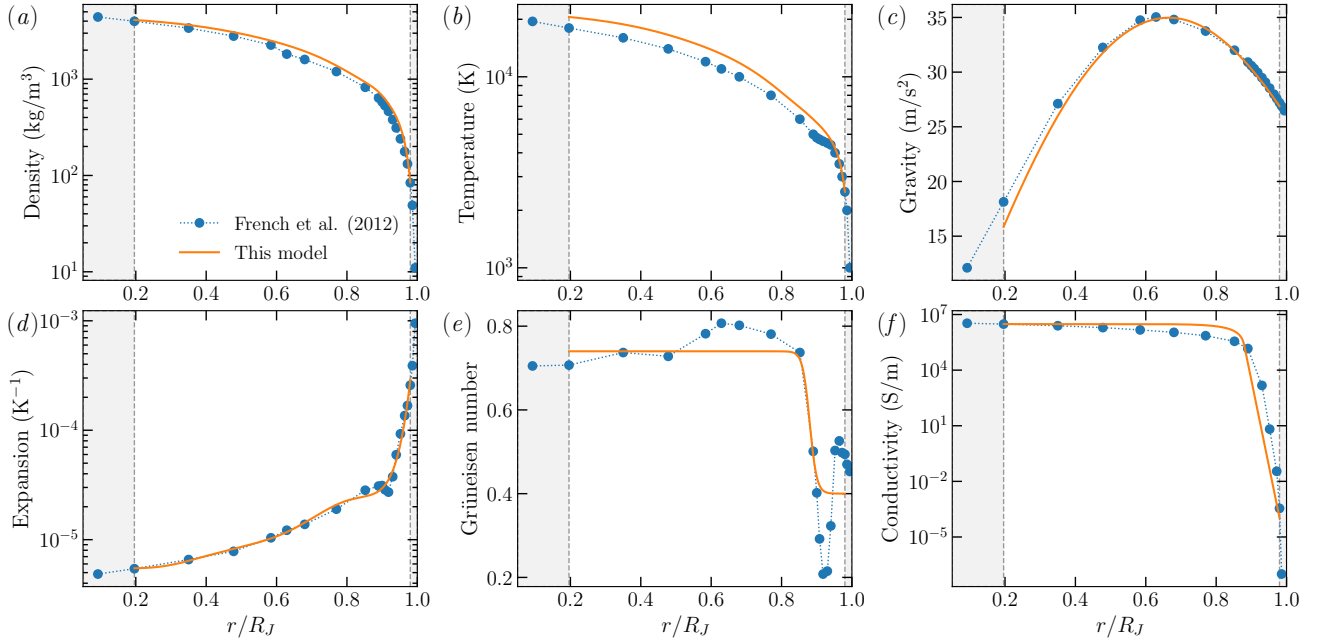


**Figure 3:** Comparison of the reference state considered in this study (solid lines in all panels) using  $Di = 28.417$ ,  $Co = 0.73$  and  $\Gamma_o = 0.4$  with the *ab initio* models from French et al. (2012) (dashed lines in all panels). (a) Background density profile as a function of the normalised radius  $r/R_J$ . (b) Background temperature profile as a function of the normalised radius. (c) Gravity profile as a function of the normalised radius. (d) Thermal expansion coefficient as a function of the normalised radius. (e) Grüneisen number as a function of the normalised radius. (f) Electrical conductivity as a function of the normalised radius. (c). The reference model employed in the numerical simulations spans from  $0.196 R_J$  to  $0.98 R_J$ . Those boundaries are highlighted by gray shaded areas on each panel. The conversion between dimensional and dimensionless units is done by simple multiplication by the reference values expressed in Tab. 1.

Fixing  $s'$  at the outer boundary grossly reflects the entropy mixing in the neglected outer 2% of Jupiter. The material outside the simulated spherical shell is assumed to be electrically insulating. Hence, the magnetic field matches a potential field at both boundaries.

## 2.5. Numerical methods

The dynamo model presented in this study has been computed using the open-source MHD code `MagIC` (freely available at <https://github.com/magic-sph/magic>, see Wicht, 2002). `MagIC` has been tested and validated against several anelastic benchmarks (Jones et al., 2011). The set of equations (7-10) complemented by the boundary conditions (15-16) is solved in spherical coordinates by expanding the velocity and the magnetic fields into poloidal and toroidal potentials:

$$\begin{aligned} \tilde{\rho} \mathbf{u} &= \nabla \times (\nabla \times W \mathbf{e}_r) + \nabla \times Z \mathbf{e}_r, \\ \mathbf{B} &= \nabla \times (\nabla \times G \mathbf{e}_r) + \nabla \times H \mathbf{e}_r. \end{aligned} \quad (17)$$

The quantities  $W$ ,  $Z$ ,  $G$ ,  $H$ ,  $s'$  and  $p'$  are expanded in spherical harmonics up to a degree  $\ell_{\max}$  in the angular directions and in Chebyshev polynomials up to the degree  $N_c$  in the radial direction. For the latter, a Chebyshev collocation method is employed using the Gauss-Lobatto interval with

$N_r$  grid points defined by

$$x_k = \cos \left[ \frac{(k-1)\pi}{N_r-1} \right], \quad k \in [1, N_r].$$

This interval that ranges between  $-1$  and  $1$  is usually directly remapped onto  $[r_i, r_o]$  by using a simple affine mapping (e.g. Glatzmaier, 1984, p. 468). However, because of the clustering of grid points in the vicinity of the boundaries, the Gauss-Lobatto grid features a minimum grid spacing that decays with  $N_r^{-2}$ . The propagation of Alfvén waves close to the boundaries then imposes severe restrictions on the time step size (Christensen, Olson and Glatzmaier, 1999). To alleviate this limitation, we rather employ the mapping by Kosloff and Tal-Ezer (1993) defined by

$$r_k = \frac{r_o - r_i}{2} \frac{\arcsin(\alpha_{\text{map}} x_k)}{\arcsin \alpha_{\text{map}}} + \frac{r_o + r_i}{2}, \quad k \in [1, N_r].$$

To ensure the spectral convergence of the collocation method, the mapping coefficient  $\alpha_{\text{map}}$  has to be kept under a maximum value that depends on  $N_r$ ,

$$\alpha_{\text{map}} \leq \left[ \cosh \left( \frac{|\ln \epsilon_m|}{N_r - 1} \right) \right]^{-1},$$

where  $\epsilon_m$  is the machine precision (Kosloff and Tal-Ezer, 1993).

**Table 2**

Definitions and estimates of dimensionless parameters in Jupiter's interior along with values adopted in the numerical model. Estimates for Jupiter have been obtained using the dimensional values from Tab. 1. The deviation from the adiabat  $\epsilon_s$  has been obtained by using a simple thermal wind balance  $\epsilon_s \sim \Omega u / \alpha_o g_o T_o$  (see Jones, 2015). The estimates of the degree of stratification and the location of a possible SSL in Jupiter come from Militzer et al. (2016) and Debras and Chabrier (2019). The mean density  $\rho_m = 1300 \text{ kg/m}^3$  and the mean magnetic diffusivity  $\lambda_m = 1.15 \text{ m}^2/\text{s}$  come from French et al. (2012).

Symbol	Name	Definition	Jupiter	This model
$Di$	Dissipation	$\alpha_o T_o g_o / c_p$	29.8	28.42
$Co$	Compressibility	$\alpha_o T_o$	0.645	0.73
$\Gamma_o$	Grüneisen		0.470	0.4
$\epsilon_s$	Adiabaticity	$d  ds/dr _{r_o} / c_p$	$\mathcal{O}(10^{-6})$	$10^{-4}$
$\mathcal{R}_i$	SSL inner radius		$0.8 - 0.9 R_J$	$0.82 R_J$
$\mathcal{R}_o$	SSL outer radius		$0.88 - 0.93 R_J$	$0.86 R_J$
$N_m / \Omega$	Degree of stratification		1 – 3	10.4
$Ra$	Rayleigh	$\alpha_o T_o g_o d^4  ds/dr _{r_o} / \nu \kappa c_p$	$10^{31}$	$3.7 \times 10^{10}$
$E$	Ekman	$\nu / \Omega d^2$	$10^{-18}$	$10^{-6}$
$Pr$	Prandtl	$\nu / \kappa$	$10^{-2} - 1$	0.2
$Pm$	Magnetic Prandtl	$\nu / \lambda_i$	$10^{-6}$	0.4
$Rm$	Magnetic Reynolds	$u d / \lambda_i$	$\mathcal{O}(10^6)$	$4.11 \times 10^2$
$Re$	Reynolds	$u d / \nu$	$\mathcal{O}(10^{12})$	$6.23 \times 10^3$
$Ro$	Rossby	$u / \Omega d$	$\mathcal{O}(10^{-6})$	$6.23 \times 10^{-3}$
$Re_Z$	Zonal Reynolds	$u_z d / \nu$	$\mathcal{O}(10^{12} - 10^{15})$	$5.79 \times 10^3$
$Re_c$	Convective Reynolds	$u_c d / \nu$	$\mathcal{O}(10^{12})$	$2.33 \times 10^3$
$\Lambda$	Elsasser	$B^2 / \rho_m \lambda_m \mu_0 \Omega$	$\mathcal{O}(10^1 - 10^2)$	8.52
$\overline{E_M} / \overline{E_K}$	Energy ratio	$B^2 / \mu_0 \rho_m u^2$	$\mathcal{O}(10^2 - 10^3)$	3.50
$f_{ohm}$	Ohmic fraction	$\overline{D_\lambda} / (\overline{D_\lambda} + \overline{D_\nu})$	1	0.78
$f_{dip}$	Axial-dipole fraction	$B_{\ell=1, m=0}^2(R_J) / B_{\ell, m \leq 12}^2(R_J)$	0.75	0.95

The equations are advanced in time using an implicit-explicit Crank-Nicolson Adams-Bashforth second order scheme, which handles the nonlinear terms and the Coriolis force explicitly and the remaining terms implicitly (Glatzmaier, 1984). Because of the stable stratification, the advection of the background entropy gradient,  $u_r d\tilde{s}/dr$ , that enters Eq. (10) is also handled implicitly to avoid severe time step restrictions when the Brunt-Väisälä frequency exceeds the rotation rate (see Brown, Vasil and Zweibel, 2012). MagIC uses the open-source library SHTns (freely available at <https://bitbucket.org/nschaeff/shtns>, see Schaeffer, 2013) for the spherical harmonic transforms. A more comprehensive description of the numerical method can be found in Glatzmaier (1984), Tilgner (1999) or Christensen and Wicht (2015).

## 2.6. Control parameters

The formation of zonal flows in global spherical models requires a combination of strong turbulent convective motions (i.e. large Reynolds numbers) and rapid rotation (i.e. low Rossby numbers). This regime, frequently referred to as the *quasi-geostrophic turbulent regime* of convection (e.g. Julien, Knobloch, Rubio and Vasil, 2012), can only be reached a low enough Ekman numbers, where global numerical simulations become extremely demanding. We therefore focus here on one single global dynamo model with  $E = 10^{-6}$ ,  $Ra = 3.7 \times 10^{10}$ ,  $Pm = 0.4$ ,  $Pr = 0.2$ . We adopted a spatial resolution of  $N_r = 361$  (with

$\alpha_{map} = 0.994$ ) and  $\ell_{max} = 597$  for most of the run. For the alias-free mapping used in the horizontal directions, this corresponds to  $N_\theta = 896$  latitudinal grid points and  $N_\phi = 1792$  longitudinal grid points. Spatial convergence of the solution has been tested by increasing the angular resolution to  $\ell_{max} = 1024$  ( $N_\phi = 3072$ ) towards the end of the run, without any noticeable change in the average properties. To ease the transients, the numerical model was initiated from another dynamo simulation computed at a larger Ekman number, and mild hyper-diffusion of the velocity and entropy fields were used over the first half of the computation time before their gradual removal (e.g. Kuang and Bloxham, 1999).

In rapidly-rotating convection (e.g. Takehiro and Lister, 2001; Dietrich and Wicht, 2018; Gastine et al., 2020), the distance of penetration  $\delta$  of a convective eddy of size  $d_c$  is directly related to the ratio of the Brunt-Väisälä frequency to the rotation rate via

$$\delta = \left( \frac{N_m}{\Omega} \right)^{-1} d_c. \quad (18)$$

Ensuring that  $\delta$  remains smaller than the thickness of the SSL  $\mathcal{H}_s$  requires  $N_m / \Omega > d_c / \mathcal{H}_s$ . A thinner layer would thus require a stronger stratification or a slower rotation to remain effective. Here we adopt  $\mathcal{H}_s = 0.05$  and  $N_m / \Omega \simeq 10.4$  ( $\Gamma_s = 2000$ ). The strong degree of stratification should suffice to stop even very large eddies of half the system size,  $d_c \simeq 0.5 d$ . While thinner and shallower stable layers



may be compatible with gravity observations, they would also considerably increase the numerical costs. Increasingly fine spatial grids are required to resolve the dynamics of thinner layers. Moreover, the tendency to form multiple jets increases with decreasing Ekman number. Relevant here is the effective Ekman number of the outer layer  $E_o = E(d/d_o)^2$  with  $d_o = r_o - R_o$ . Multiple jets may start to form below  $E_o \approx 10^{-4}$  (e.g. Jones and Kuzanyan, 2009; Gastine et al., 2014a), a value barely reached for  $d_o = 0.12$  and  $E = 10^{-6}$ .

The upper parts of Tab. 2 summarises our control parameters as well as the corresponding values for Jupiter.

Because of its significant numerical cost, the dynamo model has been integrated for a bit more than 0.13 magnetic diffusion time (or 8400 rotation periods), which required roughly 3 million core hours on Intel Haswell CPUs.

## 2.7. Diagnostics

We analyse the numerical solution by defining several diagnostic properties. In the following, triangular brackets denote volume averaging, square brackets azimuthal averaging and overlines time averaging

$$\langle f \rangle = \frac{1}{V} \int_V f dV, [f] = \frac{1}{2\pi} \int_0^{2\pi} f d\phi, \bar{f} = \frac{1}{\tau} \int_{t_o}^{t_o+\tau} f dt,$$

where  $\tau$  is the averaging interval and  $V$  is the spherical shell volume. Since the background state strongly varies with radius, it is also convenient to explore averages over a spherical surface

$$\|f\|(r, t) = \int_0^{2\pi} \int_0^\pi |f| \sin\theta d\theta d\phi.$$

The typical convective flow amplitude is measured by the Reynolds number  $Re$ , the Rossby number  $Ro$  or the magnetic Reynolds number  $Rm$  defined by

$$Re = \sqrt{\langle u^2 \rangle}, \quad Ro = Re E, \quad Rm = \frac{1}{V} \int_{r_i}^{r_o} \frac{\sqrt{\|u\|^2}}{\tilde{\lambda}} r^2 dr. \quad (19)$$

To better separate the different flow components, we define two additional measures based on the zonal flow velocity,  $Re_z$ , and on the convective flow velocity,  $Re_c$ :

$$Re_z = \sqrt{\langle [u_\phi]^2 \rangle}, \quad Re_c = \sqrt{Re^2 - Re_z^2}. \quad (20)$$

The magnetic field amplitude is characterised by the Elsasser number

$$\Lambda = \left\langle \frac{B^2}{\tilde{\rho} \tilde{\lambda}} \right\rangle. \quad (21)$$

The geometry of the surface magnetic field is expressed by its axial dipolar fraction  $f_{dip}$ , which is defined as the ratio

of the energy of the axisymmetric dipole component to the magnetic energy in the spherical harmonic degrees  $\ell \leq 12$  at  $r_o$  (Christensen and Aubert, 2006).

The numerical solution is also examined in terms of its power budget. Taking the inner product of the Navier-Stokes equation (8) by  $\mathbf{u}$  and the induction equation (9) by  $\mathbf{B}$  yields

$$\frac{d}{dt} (E_K + E_M) = \mathcal{P} - D_v - D_\lambda. \quad (22)$$

In the above equation,  $E_K$  and  $E_M$  denote the mean kinetic and magnetic energy densities

$$E_K(t) = \frac{1}{2} \langle \tilde{\rho} u^2 \rangle, \quad E_M(t) = \frac{1}{2} \frac{1}{E Pm} \langle B^2 \rangle,$$

$\mathcal{P}$  is the buoyancy power density

$$\mathcal{P}(t) = \frac{RaE}{Pr} \langle \tilde{\alpha} \tilde{T} \tilde{g} s' u_r \rangle,$$

and  $D_v$  and  $D_\lambda$  the power dissipated by viscous and Ohmic effects

$$D_v(t) = \langle S^2 \rangle, \quad D_\lambda(t) = \frac{1}{E Pm^2} \langle \tilde{\lambda} j^2 \rangle.$$

Once a statistically-steady state has been reached, time averaging Eq. (22) yields a balance between buoyancy input power and heat losses by Ohmic and viscous dissipations

$$\overline{\mathcal{P}} - \overline{D_v} - \overline{D_\lambda} = \overline{\mathcal{P}} - \frac{1}{f_{ohm}} \overline{D_\lambda} = 0, \quad (23)$$

where  $f_{ohm}$  quantifies the fraction of heat dissipated ohmically. The residual in the above equation can serve as a good indicator of the time and spatial convergence of a numerical solution (e.g. King, Stellmach and Aurnou, 2012, their Fig. 2). Here, this identity is obtained to a high degree of fidelity with  $|\overline{\mathcal{P}} - \overline{D_v} - \overline{D_\lambda}|/\overline{\mathcal{P}} < 0.3\%$ .

Table 2 summarises the control parameters and the main diagnostics of the dynamo model presented here along with the expected values for Jupiter. For comparison we note that the Jovian dynamo model by Gastine et al. (2014b) was computed using  $Pm = 0.6$  and  $E = 10^{-5}$ . It produced a relatively weak-field solution with  $\overline{E_M}/\overline{E_K} \simeq 0.1$  and  $f_{ohm} \simeq 0.15$ . In contrast, by employing much larger magnetic Prandtl number ( $Pm \geq 3$ ), several dynamo simulations by Jones (2014) and Duarte et al. (2018) yielded a stronger magnetic field with  $\overline{E_M}/\overline{E_K} \simeq 3$ . Adopting a significantly lower Ekman number enables us to reach a comparable energy fraction  $\overline{E_M}/\overline{E_K} \simeq 3.5$  while using a magnetic Prandtl number almost one order of magnitude smaller. This yields an Ohmic fraction  $f_{ohm} \simeq 0.8$ , much closer to the value expected for Jupiter where Ohmic dissipation dominates by far because of the small magnetic Prandtl number. Using  $E = 10^{-6}$  also ensures that  $Re \gg 1$  and yet  $Ro \ll 1$ , two prerequisites to develop turbulent quasi-geostrophic convection conducive for sustaining strong zonal jets.

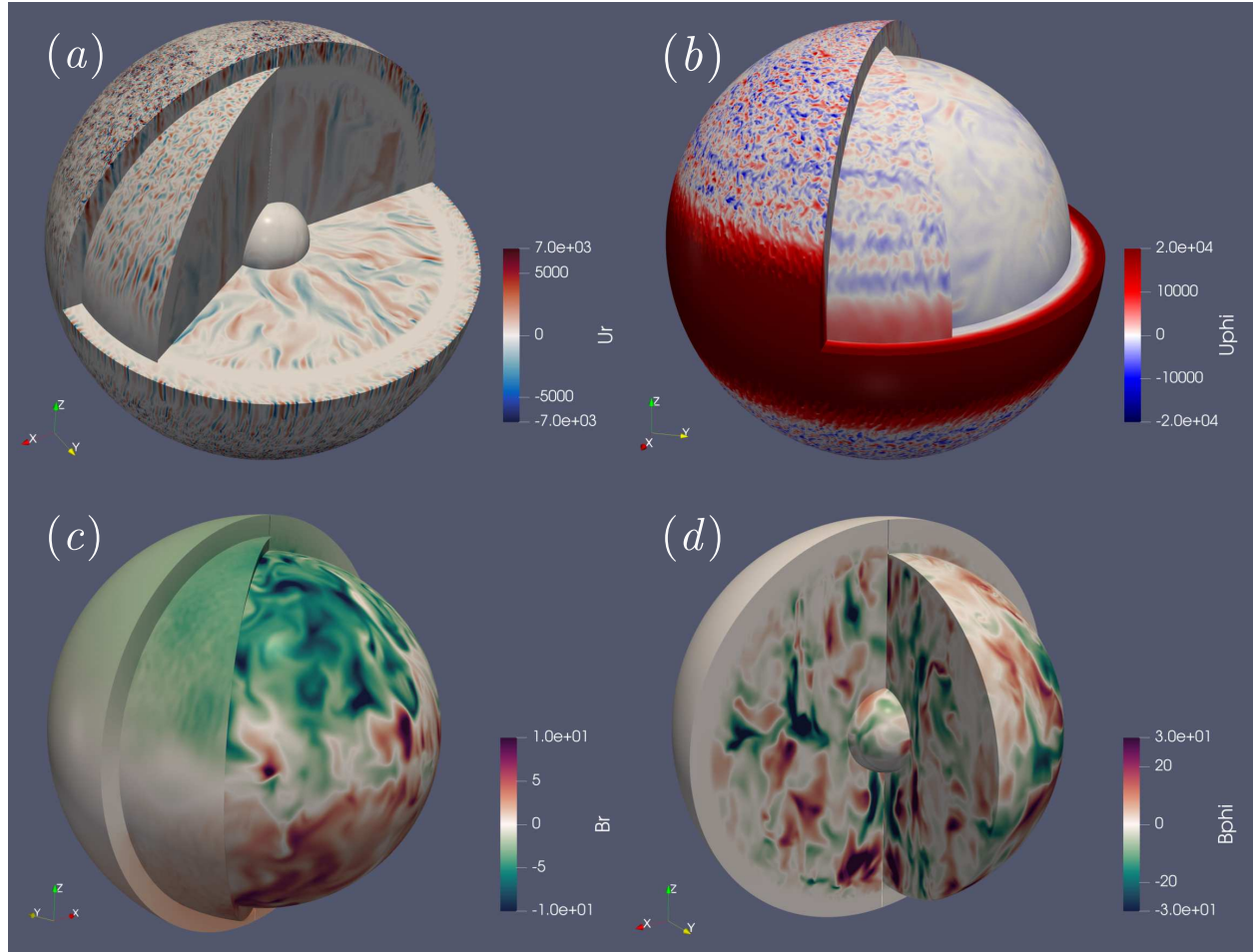


**Figure 4:** 3-D renderings of the radial velocity  $u_r$  (a), of the azimuthal velocity  $u_\phi$  (b), of the radial component of the magnetic field  $B_r$  (c) and of the azimuthal component of the magnetic field  $B_\phi$  (d). The inner sphere in panels (a) and (d) is located very close to the inner boundary at  $r = r_i + 0.01$ , while in panel (b) and (c) it depicts the lower boundary of the SSL. The intermediate radial cut that spans  $30^\circ$  in longitude in panels (a)-(c) and  $90^\circ$  in panel (d) is located close to the upper boundary of the stably-stratified layer at  $r = 0.904 r_o$ . The external radial cut corresponds to  $r = 0.992 r_o$  in panel (a) and to the surface  $r_o$  in the other panels.

### 3. Results

#### 3.1. Convective flow and magnetic field morphology

We start by examining the typical convective flow and magnetic field produced by the numerical dynamo model. Figure 4 shows a selected snapshot of the radial and azimuthal components of the velocity and magnetic fields. An immediate effect of the strong stratification  $N_m/\Omega \simeq 10$  is to significantly inhibit the convective motions between  $\mathcal{R}_i$  and  $\mathcal{R}_o$ . The equatorial and meridional cuts of the radial velocity (Fig. 4a) clearly show that the SSL forms a strong dynamical barrier between two different convective regions. In the deep interior, the convective pattern takes the form of radially-elongated quasi-geostrophic sheets that span most of the metallic core. This is a typical flow pattern commonly observed in geodynamo models when the magnetic energy exceeds the kinetic energy (e.g. Yadav, Gastine, Christensen, Wolk and Poppenhaeger, 2016, their Fig. 2). In contrast,

the outer layer is dominated by small-scale turbulent features. Because of the rapid decrease of density there, the convective flow become smaller-scale and more turbulent towards the surface. The azimuthal flows are dominated by a strong prograde equatorial jet which penetrates down to  $\mathcal{R}_o$  (Fig. 4b) but are then effectively quenched in the stable layer. Flanking weaker jets of alternating direction appear up to about  $\pm 40^\circ$  in latitude. They become somewhat more pronounced with depth and show clearer at  $r = 0.9 r_o$  ((radial cut in Fig. 4b)

The magnetic field is predominantly produced in the metallic region below  $\mathcal{R}_i$  where both the conductivity and the convective flow amplitude are sufficient to sustain dynamo action (Fig. 4c-d). The magnetic Reynolds number (Eq. 19) reaches values of more than 600 in this region. The magnetic field at the top of the inner convective region features a dominant axisymmetric dipole accompanied by intense localised flux patches (inner radial cut in Fig. 4c). Because of the strong inhibition of the flow motions between

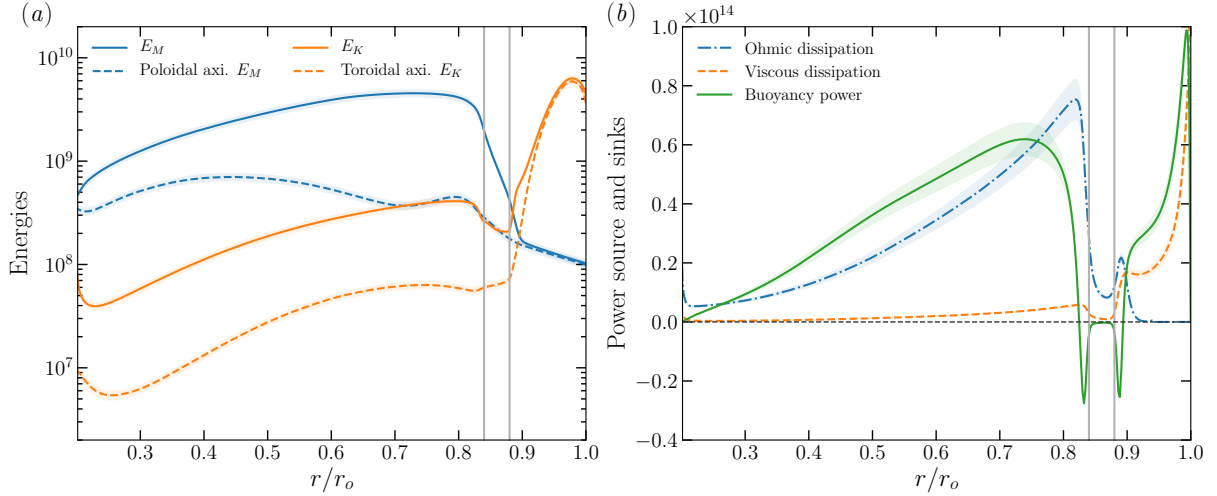


**Figure 5:** (a) Time-averaged radial profiles of magnetic and kinetic energies. (b) Time-averaged radial profiles of Ohmic and viscous dissipation and buoyancy power. The shaded area correspond to one standard-deviation across the mean. The vertical lines mark the location of the stably-stratified layer between  $\mathcal{R}_i$  and  $\mathcal{R}_o$  (see Fig. 2).

$\mathcal{R}_i$  and  $\mathcal{R}_o$ , there is little to no dynamo action happening in the SSL. Instead, the SSL filters out the faster varying field components via a magnetic skin effect as will be discussed in the next section (e.g. Christensen, 2006; Gastine et al., 2020). Since smaller scale contributions vary on shorter time scales, the remaining field at  $\mathcal{R}_o$  is of much larger scale than at  $\mathcal{R}_i$ .

Because of the abrupt drop of electrical conductivity in the molecular envelope, the dynamo action in the outer layer is very inefficient since the magnetic Reynolds number  $Rm$  is mostly smaller than one in the outer convective layer of our simulation. Consequently, the locally-induced poloidal field remains practically negligible and the magnetic field decays like a potential field with radius (Wicht et al., 2019b). The surface magnetic field is dominated by a strong axial dipole combined with large scale non-axisymmetric flux patches. In the fully-convective models by Gastine et al. (2014b), the prograde equatorial jet shears the upper layers of the metallic region to produce strong azimuthal magnetic bands (Wicht et al., 2019b). Such structures are not observed here (Fig. 4d), likely because the zonal motions are hampered in the stable layer.

### 3.2. Energetics

For a more quantitative assessment, we now examine the power balance. Figure 5 shows the time-averaged radial profiles of magnetic and kinetic energy as well as the different source and sinks which enter the power balance (22). In the metallic interior, the total magnetic energy exceeds the kinetic energy by one order of magnitude and zonal winds (toroidal axisymmetric) contribute only about 10% of the kinetic energy (Fig. 5a). In the SSL, the total kinetic energy drops with radius by about a factor of two. Non-axisymmetric contributions drop more rapidly, but this is partly compensated by an increase in the zonal kinetic energy due to penetration from the upper convective region.

In the external convective layer, fast zonal winds clearly dominate and the kinetic energy reaches its peak value at about  $0.98 r_o$ . Because of the skin-effect in the SSL and the decay of conductivity, the magnetic field becomes more axisymmetric and poloidal towards the surface. While kinetic and magnetic energy reach a comparable level at the top of the SSL, the former exceeds the latter by up to a factor 50 in the outer convective layer.

The sign changes of the buoyancy power (Fig. 5b) mark the actual separation between the convective and the stably-stratified layers. In the convective regions, the eddies which carry a positive entropy fluctuation compared to their surroundings ( $s' > 0$ ) rise outwards, while the ones with  $s' < 0$  sink inwards, yielding a positive correlation between  $u_r$  and  $s'$  and hence a positive buoyancy power. The opposite happens when a convective feature overshoots in an adjacent sub-adiabatic region. A rising parcel of fluid with  $u_r > 0$  now carries a perturbation  $s' < 0$  (and hence  $\mathcal{P} < 0$ ) until it is homogenised with its surroundings by heat conduction ( $\mathcal{P} \approx 0$ ). Because of the finite stiffness of the background entropy gradient (Fig. 2), the actual thickness of the region with  $\mathcal{P} < 0$  exceeds the interval  $[\mathcal{R}_i, \mathcal{R}_o]$  delineated by vertical lines in Fig. 5. The measure of the vertical extent of the regions with  $\mathcal{P} < 0$  actually provide a good estimate of the distance of penetration of the convective eddies into a stably-stratified layer (e.g. Browning et al., 2004; Takehiro and Sasaki, 2018; Gastine et al., 2020).

In line with the partitioning between magnetic and kinetic energies, the heat losses are dominated by Ohmic heating in the metallic region, while viscous heating takes over when the electrical conductivity drops. To sum up, Fig. 5 highlights the separation between two different dynamical regions: an internal metallic region, which harbours the production of a strong magnetic field, and an external envelope where most of the kinetic energy is pumped into zonal motions.

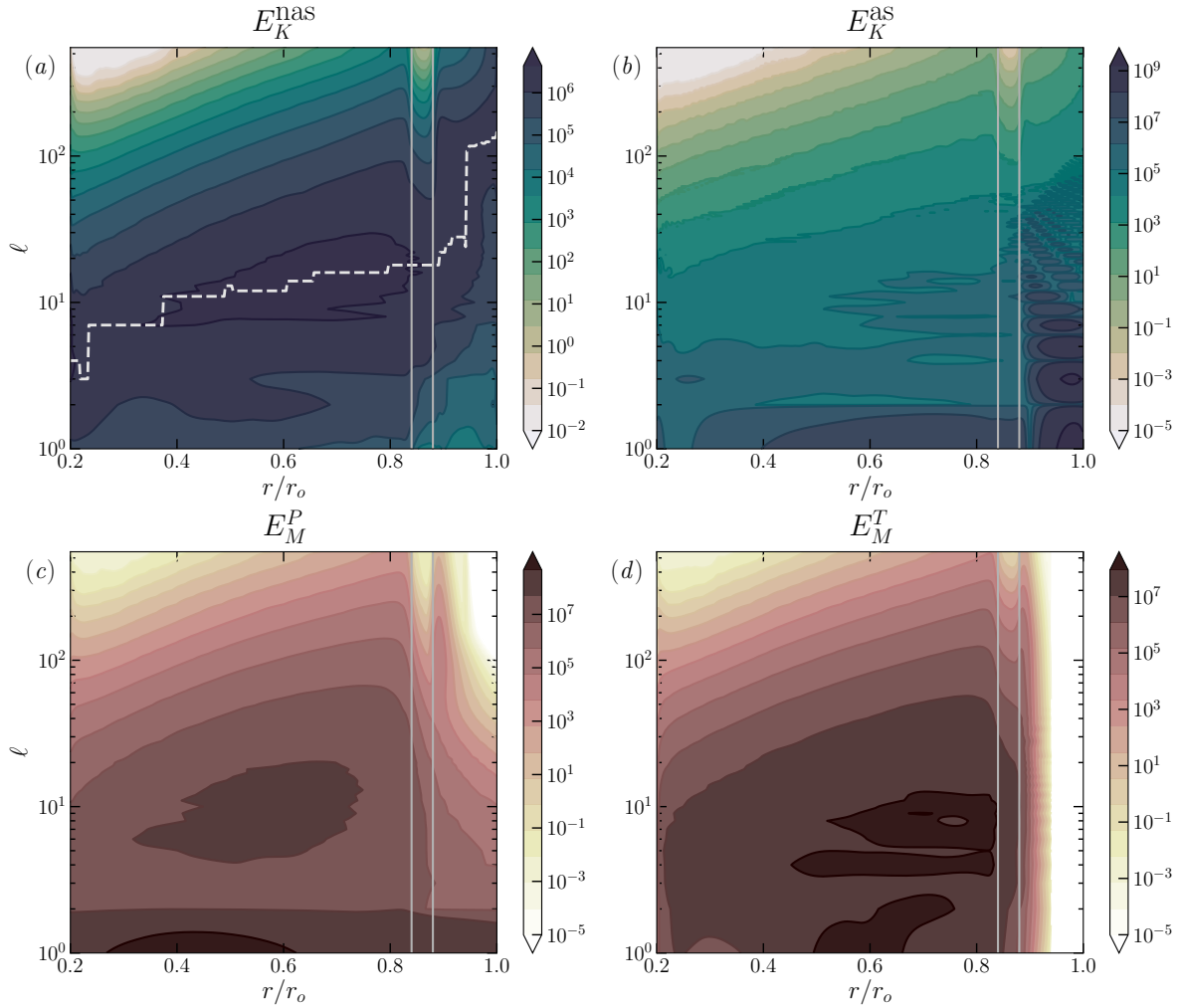


**Figure 6:** Time-averaged 2-D spectra in  $(r/r_o, \ell)$  plane for several kinetic (upper panels) and magnetic (lower panels) contributions: (a) non-axisymmetric kinetic energy, (b) axisymmetric kinetic energy, (c) poloidal magnetic energy, and (d) toroidal magnetic energy. The thick dashed line in panel (a) mark the location of the maxima of non-axisymmetric kinetic energy. The solid lines mark the location of the stably-stratified layer between  $\mathcal{R}_i$  and  $\mathcal{R}_o$  (see Fig. 2). Because of the different dynamics, the colorbars are different for each panel.

To better characterise the dynamics in the different layers, we now examine the spectral energy distributions in the  $(r/r_o, \ell)$  plane. Figure 6 illustrates 2-D spectra of kinetic (upper panels) and magnetic (lower panels) energy contributions. For a more insightful analysis, the kinetic energy has been split into non-axisymmetric (Fig. 6a) and axisymmetric (Fig. 6b) motions, while the magnetic spectra have been separated into poloidal (Fig. 6c) and toroidal (Fig. 6d) contributions.

We introduce the local peak of the non-axisymmetric energy  $\hat{\ell}$  and the corresponding convective flow lengthscale  $d_c$  defined by

$$\hat{\ell}(r) = \operatorname{argmax}_{\ell} E_K^{\text{nas}}, \quad d_c(r) = \frac{\pi r}{\hat{\ell}}, \quad (24)$$

where  $E_K^{\text{nas}}$  denotes the non-axisymmetric energy (e.g. Schwaiger, Gastine and Aubert, 2019). The kinetic energy spectra clearly differ for the three regions. In the external layers ( $r > \mathcal{R}_o$ ), the convective lengthscale rapidly decreases

outwards, reaching  $\hat{\ell} \sim 100$ , i.e.  $d_c \approx 0.03 r_o$ . The scale of the zonal flows remains roughly an order of magnitude larger with  $\ell \leq 20$ . In the metallic core ( $r < \mathcal{R}_i$ ),  $\hat{\ell}$  decreases only mildly from about 15 at  $\mathcal{R}_i$  to about 4 at  $r_i$ . In the physical space this corresponds to the large scale convective sheets visible in Fig. 4a. In between those two regions, the stably-stratified layer significantly reduces the amplitude of the convective motions. The inhibition of the convective flow depends on the size of the convective eddies: the smaller the lengthscale, the stronger the attenuation of the kinetic energy. This phenomenon can be understood when considering the distance of penetration  $\delta$  of a turbulent feature of horizontal size  $d_c$  into a stably stratified layer (Eq. 18). Approximating the horizontal scale  $d_c$  by  $\pi \mathcal{R}_i / \ell$  then yields

$$\delta_{\ell} \sim \frac{\pi}{\mathcal{R}_i} \left( \frac{N_m \ell}{\Omega} \right)^{-1}. \quad (25)$$

The penetration distance  $\delta_\ell$  is hence inversely proportional to the degree  $\ell$ , explaining the stronger damping of small convective scales (Dietrich and Wicht, 2018). At the dominant lengthscale of convection  $\hat{\ell} \simeq 20$  at the edges of the SSL, the above scaling yields  $\delta_{\hat{\ell}} \simeq 0.015 d$ , in good agreement with the actual thickness of the overshoot regions characterised by  $\mathcal{P} < 0$  (Fig. 3b).

The poloidal magnetic energy is dominated by its dipolar component throughout the entire volume. In the metallic interior, it features a secondary peak around  $\ell \simeq 10 - 20$  which roughly follows the variations of the peak of the non-axisymmetric kinetic energy  $\hat{\ell}(r)$  (Aubert, Gastine and Fournier, 2017). The toroidal field reaches its maximum amplitude in the upper half of the metallic core ( $0.6 \leq r \leq \mathcal{R}_i$ ) and also peaks at comparable scales. Beyond  $\mathcal{R}_i$ , the magnetic energy decreases up to the surface  $r_o$  and is significantly more attenuated at small scales. This phenomenon arises because of two distinct scale-dependent physical processes:

1. Within the SSL, the electrical conductivity is almost as large as in the metallic core but the convective motions are significantly hampered. A first order approximation assumes that the SSL behaves as a stagnant layer of size  $\mathcal{H}_s$  with a constant electrical conductivity. Such a layer will attenuate the poloidal magnetic energy by *skin effect* (e.g. Christensen, 2006) by a factor

$$\ln \frac{E_M^{P,\ell}(\mathcal{R}_o)}{E_M^{P,\ell}(\mathcal{R}_i)} \sim -\frac{\mathcal{H}_s}{\delta_\ell^{\text{SK}}}, \quad (26)$$

where  $E_M^{P,\ell}$  is the poloidal magnetic energy at the harmonic degree  $\ell$  and  $\delta_\ell^{\text{SK}}$  is the skin depth associated with a feature of scale  $d_c$  expressed by (see Gastine et al., 2020)

$$\delta_\ell^{\text{SK}} \sim \left(\frac{d_c}{Rm}\right)^{1/2} \sim \left(\frac{\pi \mathcal{R}_i}{\ell Rm}\right)^{1/2}. \quad (27)$$

The skin effect (26) thus increases with  $\ell$ .

2. Beyond  $\mathcal{R}_o$ , the electrical conductivity decreases exponentially and the local dynamo effect is rather inefficient. The magnetic field is dominated by the field produced in the deeper dynamo region and approaches a potential field (e.g. Wicht et al., 2019b). The characteristic radial dependence of a potential field in the outer convective region predicts:

$$\frac{E_M^{P,\ell}(r_o)}{E_M^{P,\ell}(\mathcal{R}_o)} \simeq \left(\frac{\mathcal{R}_o}{r_o}\right)^{2\ell+4}. \quad (28)$$

The attenuation factors (26) and (28) should provide idealised upper bounds of the poloidal magnetic energy damping since (i) the convective flows can penetrate into the SSL and (ii) the electrical conductivity beyond  $\mathcal{R}_o$  still allows for some local dynamo action. This local action is

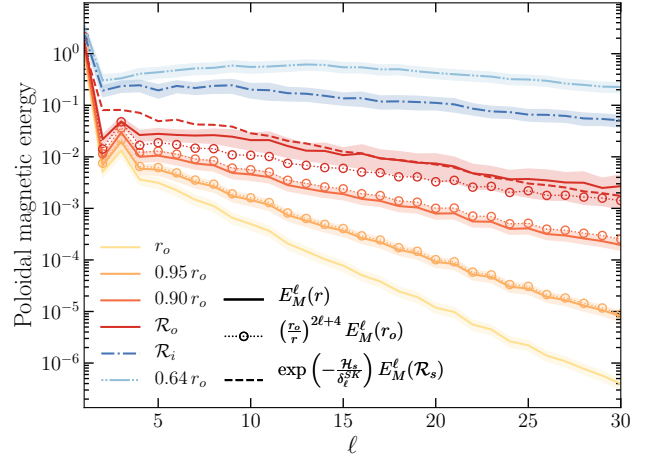


**Figure 7:** Time-averaged poloidal magnetic energy spectra at different depths up to  $\ell = 30$ . The solid (dash-dotted) lines correspond to the poloidal magnetic spectra above (below) the SSL, the circles to the downward continuation of the surface field (Eq. 28) and the dashed line to the field at  $\mathcal{R}_o$  upward-continued from  $\mathcal{R}_i$  using the skin-depth approximation (Eq. 26). The shaded regions correspond to one standard deviation across the time-averaged values.

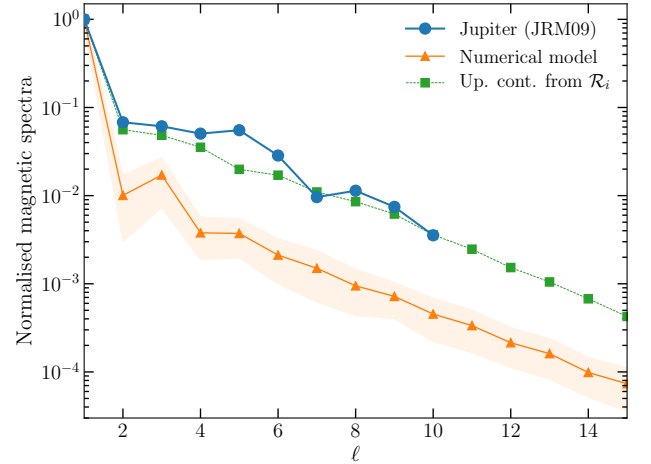


**Figure 8:** Normalised time-averaged magnetic spectra at the surface of the numerical model as well as the potential field upward continuation of the poloidal field at  $\mathcal{R}_i$  along with the Jovian magnetic field model JRM09 by Connerney et al. (2018) for the first 15 harmonic degrees. The shaded area corresponds to one standard deviation across the time-averaged values.

responsible for the rise in magnetic energy around  $\mathcal{R}_o$  at intermediate to small scales corresponding to  $\ell > 40$  (Fig. 6c-d).

Figure 7 compares spectra of the poloidal magnetic energy at different depths (solid lines) to the predictions coming from Eq. (26) (dashed lines) and Eq. (28) (circles). Beyond  $r = 0.9 r_o$ , dynamo action is negligible and the poloidal energy spectra closely follows the downward continuation of the surface field. At the top of the stable layer

( $\mathcal{R}_o = 0.88 r_o$ ), however, the energy of the downward-continued field is noticeably smaller than the actual poloidal energy. The reason is the dynamo action just above or in the top part of the stable layer, which is also apparent in Fig. 6c and d. Here the zonal winds induce toroidal field which is then converted to poloidal field by the non-axisymmetric flow components (Wicht et al., 2019b; Tsang and Jones, 2020).

Using the poloidal field spectrum at  $\mathcal{R}_i$  combined with the attenuation factor from the skin effect (26) captures the magnetic energy spectrum at  $\mathcal{R}_o$  reasonably well. Large scale contributions ( $\ell < 15$ ) are overestimated, while smaller scale contributions are slightly underestimated. The latter could be explained by the local dynamo action around  $\mathcal{R}_o$ , which intensifies the field and counteracts the skin effect. The weaker large-scale field, on the other hand, indicates that the locally-induced field opposes the field produced below the stable layer. Dipole and octupole are less affected and therefore stick out above the stable layer. Another reason for the discrepancy could be that approximating the SSL by an electrically-conducting stagnant layer is too simplistic despite the large degree of stratification considered here ( $N_m/\Omega \simeq 10$ ). In the deep interior ( $r \leq \mathcal{R}_i$ ), the octupole is in line with other spherical harmonics and the scales around  $\ell \simeq 10$  nearly reach half the amplitude of the dipole contributions (see also Fig. 6c-d).

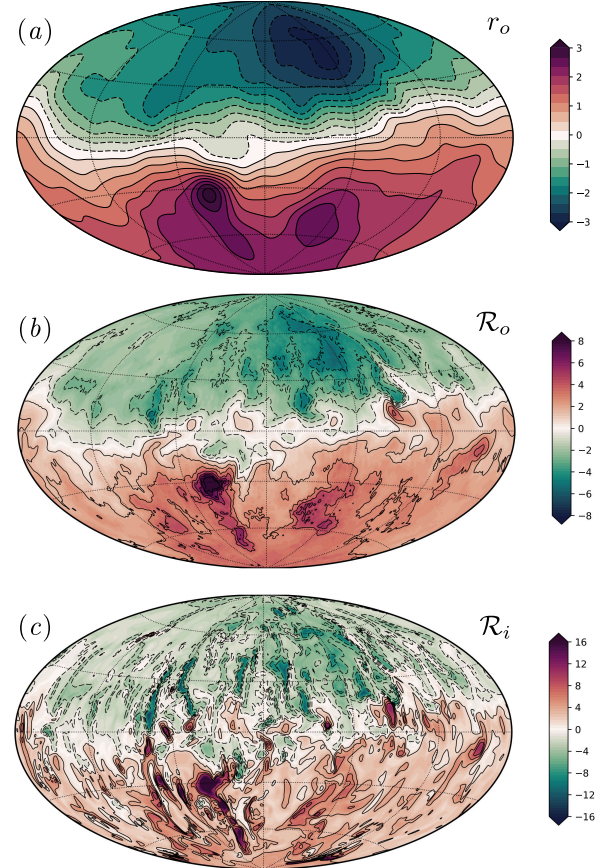
### 3.3. Comparison with JRM09

Figure 8 compares the normalised surface magnetic spectra in our simulation with the Jovian magnetic field model JRM09 by Connerney et al. (2018). The relative energy contained in the non-dipolar components is roughly one order of magnitude lower in the simulation than in the JRM09 model. The surface magnetic field produced by our dynamo model is thus too dipolar, as is illustrated by Fig. 9, which shows the radial component of the magnetic field at different depths for a snapshot of our simulation. The strong difference between northern and southern field in JRM09 (see Fig. 1) is not present in the simulation. There are some strong localised flux patches in our model, but they are more evenly distributed and do not stand out as clearly as in JRM09. From the many small scale patches at the bottom of the SSL (panel c), the strongest can still be identified at the top of the SSL (panel b) and are the origin of the larger scale patches at the outer boundary (panel a).

Figure 8 also shows an upward continuation of the poloidal magnetic field at the base of the stable layer  $\mathcal{R}_i$  using Eq. (28). This potential field approximation provides a theoretical estimate for the end-member attenuation when skin effect and dynamo action above the stable layer would be weak. The decent similarity of this approximation to the JRM09 spectrum could indicate that both are too strong in our simulation.

### 3.4. Force balances

We now turn to examining the forces that govern the numerical dynamo model. To do so, we resort to the analysis of the spectral decomposition of forces introduced by Aubert



**Figure 9:** Hammer projection of the radial component of the magnetic field at the surface (a), at the upper edge of the SSL  $r = \mathcal{R}_o$  (b) and at the lower edge of the SSL  $r = \mathcal{R}_i$  (c).

et al. (2017) and Schwaiger et al. (2019). Each force vector  $\mathbf{f}$  is expanded in vector spherical harmonics

$$\mathbf{f}(r, \theta, \phi, t) = \sum_{\ell=0}^{\ell_{\max}} Q_{\ell}^m Y_{\ell}^m \mathbf{e}_r + S_{\ell}^m r \nabla Y_{\ell}^m + \mathcal{T}_{\ell}^m \mathbf{r} \times \nabla Y_{\ell}^m, \quad (29)$$

where  $\mathbf{r}$  is the vector along the radial direction and  $Y_{\ell}^m(\theta, \phi)$  is the spherical harmonic of degree  $\ell$  and order  $m$ . The energy of the vector  $\mathbf{f}$  is then retrieved by the following identity

$$\begin{aligned} F^2 &= \int_V \mathbf{f}^2 dV, \\ &= 2 \int_{r_i}^{r_o} \sum_{\ell=0}^{\ell_{\max}} \sum_{m=0}^{\ell}{}' |Q_{\ell}^m|^2 + \ell(\ell+1) (|S_{\ell}^m|^2 + |\mathcal{T}_{\ell}^m|^2) r^2 dr, \end{aligned}$$

where the prime on the summation over the order  $m$  indicates that the  $m = 0$  coefficient is multiplied by one half. To examine the spectral distribution of the forces, the above expression is rearranged as follows:

$$F^2 = \sum_{\ell} \mathcal{F}_{\ell}^2(r_i, r_o), \quad (30)$$

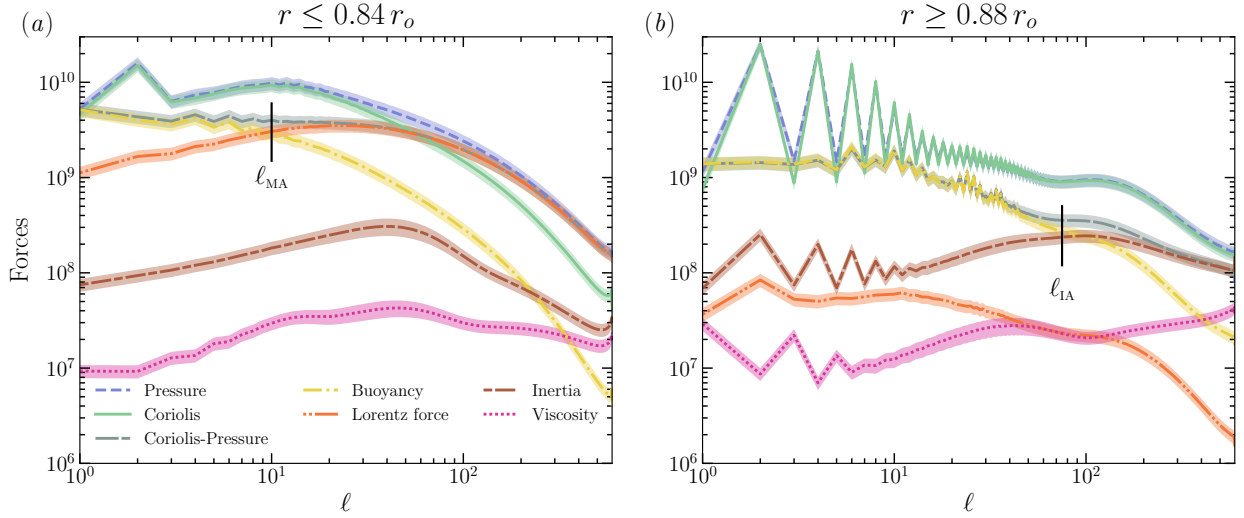


**Figure 10:** Time-averaged force balance spectra as a function of the harmonic degree integrated over the metallic core (a) and over the molecular envelope (b). The shaded area correspond to one standard-deviation across the mean. The vertical segments mark the location of the so-called “cross-over lengthscales” where three forces are in balance (see Aubert et al., 2017; Schwaiger et al., 2021).

where

$$F_\ell^2(r_b, r_t) = 2 \int_{r_b}^{r_t} \sum_{m=0}^{\ell} |Q_\ell^m|^2 + \ell(\ell+1) (|S_\ell^m|^2 + |\mathcal{T}_\ell^m|^2) r^2 dr. \quad (31)$$

We adapt the bounds of the radial integration  $r_b$  and  $r_t$  to either focus on the metallic core or on the convective envelope. Figure 10 shows the time-averaged force balance spectra  $\overline{F}_\ell(r_i, \mathcal{R}_i)$  (left) and  $\overline{F}_\ell(\mathcal{R}_o, r_o)$  (right). We find a primary geostrophic balance (QG) between pressure gradient and Coriolis force at large scales with  $\ell < 70$ . At smaller scales, the pressure gradient is superseded by Lorentz forces in a magnetostrophic balance (MS) (Aurnou and King, 2017). Beyond this primary balance, the difference between pressure gradient and Coriolis force, termed *ageostrophic Coriolis force*, is in balance with buoyancy at large scales ( $\ell < 10$ ) and with Lorentz force at small scales. Inertia and viscosity are respectively one and two orders of magnitude below this first-order balance. This forms the so-called *QG-MAC balance* (Magneto, Archimedean, Coriolis) introduced theoretically by Davidson (2013) and identified in reduced numerical models by Calkins (2018) and full dynamo simulations by Schwaiger et al. (2019). This hierarchy of forces is structurally similar to the ones obtained in the geodynamo models of Schwaiger et al. (2019) when the magnetic energy exceeds the kinetic one. We note that the separation between Lorentz force and inertia is of comparable amplitude to the ratio of magnetic and kinetic energies (see Fig. 5a).

In the molecular envelope, the leading-order quasi-geostrophic equilibrium is accompanied by a secondary balance between ageostrophic Coriolis force and buoyancy up to  $\ell \simeq 70$  and between ageostrophic Coriolis force

and inertia beyond. Because of the decrease of electrical conductivity, Lorentz forces play a much weaker role and have a comparable amplitude to the viscous force. The convective flows in the outer convective layer therefore obey the so-called *QG-IAC balance* (Inertia, Archimedean, Coriolis) derived by Cardin and Olson (1994) in the context of quasi-geostrophic convection (see also Aubert, Brito, Nataf, Cardin and Masson, 2001; Gillet and Jones, 2006; Gastine, Wicht and Aubert, 2016).

The spectral representations shown in Fig. 10 also reveal the cross-over lengthscales (Aubert et al., 2017; Schwaiger et al., 2021) defined by the harmonic degree at which at least two forces are of equal amplitude. Of particular interest are the intersections between buoyancy and Lorentz forces in the metallic core and between buoyancy and inertia in the molecular envelope. The respective degrees  $\ell_{MA} \approx 10$  and  $\ell_{IA} \approx 75$ , marked by the two vertical segments in Fig. 10, characterise the lengthscale of optimal QG-MAC and QG-IAC balances. As already reported by Aubert et al. (2017), those cross-over lengthscales are in good agreement with the dominant lengthscale of convection  $\hat{\ell}$  defined by the peak of the non-axisymmetric kinetic energy (Fig. 6a).

This implies that the most energetic convective features are controlled by a QG-MAC balance in the metallic core and a QG-IAC balance in the external convective region, two force balance hierarchies expected to hold in the interiors of gas giants.

### 3.5. Zonal and meridional flows

We now examine the structure of the axisymmetric flows produced in this numerical dynamo model. Figure 11 shows the time-averaged zonal flow  $[u_\phi]$  and the stream function  $\overline{\Psi}$  associated with the meridional circulation defined by

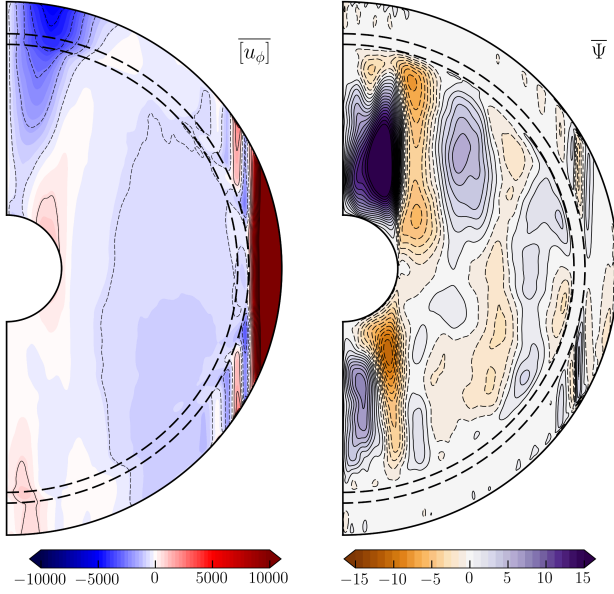


**Figure 11:** (a) Time-averaged zonal flows  $\overline{[u_\phi]}$ . (b) Time-averaged stream function of the meridional circulation  $\overline{\Psi}$ . Solid (dashed) contour lines correspond to clockwise (counter clockwise) meridional circulation. In both panels, the dashed half circles mark the bounds of the SSL  $\mathcal{R}_i$  and  $\mathcal{R}_o$ .

$$\tilde{\rho} \mathbf{u}_m = \nabla \times (\tilde{\rho} \Psi \mathbf{e}_\phi),$$

where  $\mathbf{u}_m = ([u_r], [u_\theta])$  is the meridional circulation vector and  $\mathbf{e}_\phi$  is the unit vector in the  $\phi$  direction. In the molecular envelope, the zonal motions are dominated by a strong prograde equatorial jet. On each side of the equatorial jet we find two retrograde and two prograde secondary jets. The innermost prograde jets, located at about  $40^\circ$  latitude north and south, are particularly faint. This jet system persisted over our simulation time, which is equivalent to about 8400 rotations. Zonal winds at high latitudes form broader structures, which are often dominated by thermal wind features and change over time. The deeper convective region exhibits much weaker differential rotation (see Jones, 2014).

The meridional flows are one to two orders of magnitude weaker than the typical non-axisymmetric convective flows. In the external convective region, it forms pairs of equatorially anti-symmetric cells elongated along the rotation axis. The cells are highly correlated with the zonal jets. The stable stratification effectively prevents the meridional circulations from penetrating the SSL.

Within the metallic interior, the meridional circulation resides on more intricate columnar cellular patterns which also show some correlation with the zonal winds.

In order to understand the quenching of the jets and the correlation with the meridional circulation, we consider two fundamental equations. The first one is the thermal

wind equation, which can be derived from the azimuthal component of the curl of the Navier-Stokes equation (8):

$$\begin{aligned} \frac{D\omega_\phi}{Dt} = & \frac{2}{E} \frac{\partial u_\phi}{\partial z} - \frac{Ra}{Pr} \frac{\tilde{\alpha} \tilde{T} \tilde{g}}{r} \frac{\partial s'}{\partial \theta} + \zeta \boldsymbol{\omega} \cdot \nabla \left( \frac{u_\phi}{\zeta} \right) - \omega_\phi \nabla \cdot \mathbf{u} \\ & + \mathbf{e}_\phi \cdot \nabla \times \left( \frac{\mathbf{j} \times \mathbf{B}}{EPm \tilde{\rho}} \right) + \mathbf{e}_\phi \cdot \nabla \times \left( \frac{\nabla \cdot \mathbf{S}}{\tilde{\rho}} \right). \end{aligned} \quad (32)$$

Here  $\omega_\phi = \mathbf{e}_\phi \cdot \nabla \times \mathbf{u}$  and  $\zeta = r \sin \theta$  denotes the cylindrical radius. When averaging over time and azimuth, Eq. (32) yields

$$2 \frac{\partial \overline{[u_\phi]}}{\partial z} = \frac{RaE}{Pr} \frac{\tilde{\alpha} \tilde{T} \tilde{g}}{r} \frac{\partial \overline{[s']}}{\partial \theta} + \mathcal{R}_\omega + \mathcal{M}_\omega + \mathcal{V}_\omega. \quad (33)$$

In the above equation,  $\mathcal{R}_\omega$  is a nonlinear term defined by

$$\mathcal{R}_\omega = E \left( \overline{[\mathbf{u} \cdot \nabla \omega_\phi]} - \zeta \overline{\left[ \boldsymbol{\omega} \cdot \nabla \frac{u_\phi}{\zeta} \right]} - \frac{d \ln \tilde{\rho}}{dr} \overline{[u_r \omega_\phi]} \right),$$

where the three contributions entering the right-hand-side respectively correspond to advection, stretching and compressional sources of vorticity.  $\mathcal{M}_\omega$  and  $\mathcal{V}_\omega$  denote the magnetic and viscous stresses defined by

$$\mathcal{M}_\omega = -\frac{1}{Pm} \overline{\left[ \mathbf{e}_\phi \cdot \nabla \times \left( \frac{\mathbf{j} \times \mathbf{B}}{\tilde{\rho}} \right) \right]},$$

and

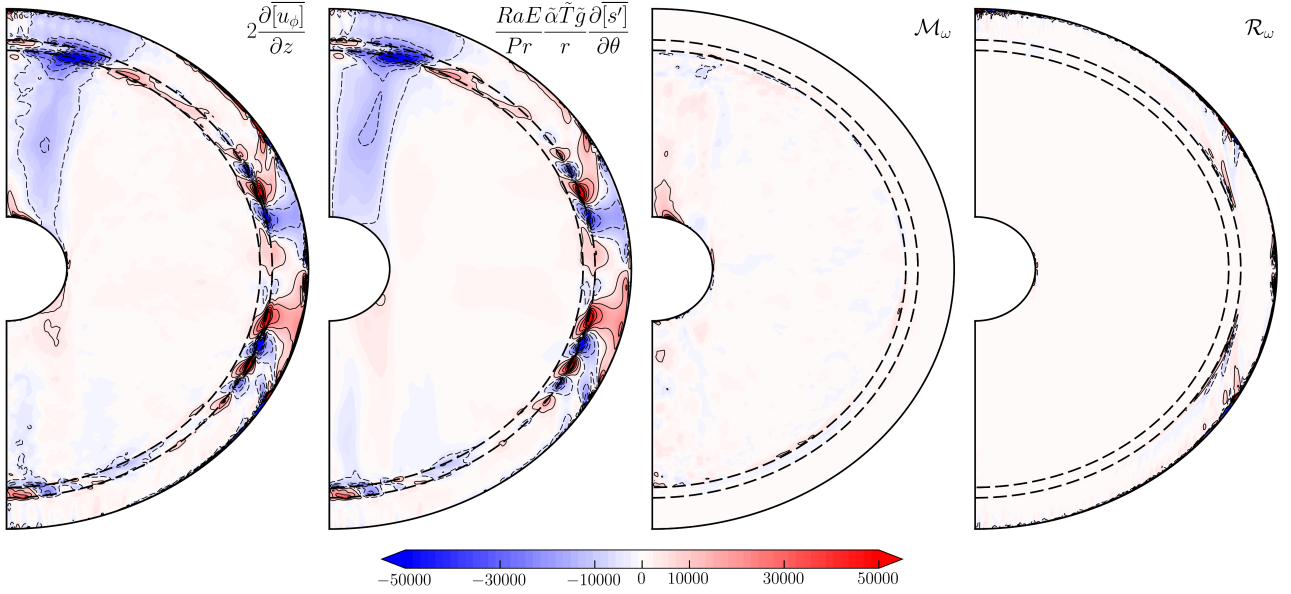
$$\mathcal{V}_\omega = -E \overline{\left[ \mathbf{e}_\phi \cdot \nabla \times \left( \frac{\nabla \cdot \mathbf{S}}{\tilde{\rho}} \right) \right]}.$$

Figure 12 shows meridional cuts of the different terms in Eq. (33). The axial gradient of  $\overline{[u_\phi]}$  almost perfectly balances the latitudinal gradient of entropy, with small remaining contributions of magnetic winds  $\mathcal{M}_\omega$  inside the tangent cylinder and from inertia close to the upper edge of the SSL around  $45^\circ$  latitude. The classical thermal wind balance

$$2 \frac{\partial \overline{[u_\phi]}}{\partial z} \approx \frac{RaE}{Pr} \frac{\tilde{\alpha} \tilde{T} \tilde{g}}{r} \frac{\partial \overline{[s']}}{\partial \theta}, \quad (34)$$

is hence realised to a high degree of fidelity, indicating that Lorentz forces have no direct impact on the  $z$ -variations of the zonal flows. The strongest latitudinal entropy gradients are found at the upper edge of the SSL between  $20^\circ$  and  $45^\circ$  latitude, where the alternating zonal flows rapidly decay. The entropy gradients are much weaker in the middle of the external convective region where the zonal winds remain nearly geostrophic. The braking of  $\overline{[u_\phi]}$  at  $\mathcal{R}_o$  is accommodated by intense localised entropy variations.





**Figure 12:** Meridional cuts of the time-averaged terms that enter the thermal wind balance (33). Because of its much weaker amplitude, the viscous contribution  $\mathcal{V}_\omega$  entering Eq. (33) has been omitted. The dashed half circles mark the bounds of the SSL  $\mathcal{R}_i$  and  $\mathcal{R}_o$ .

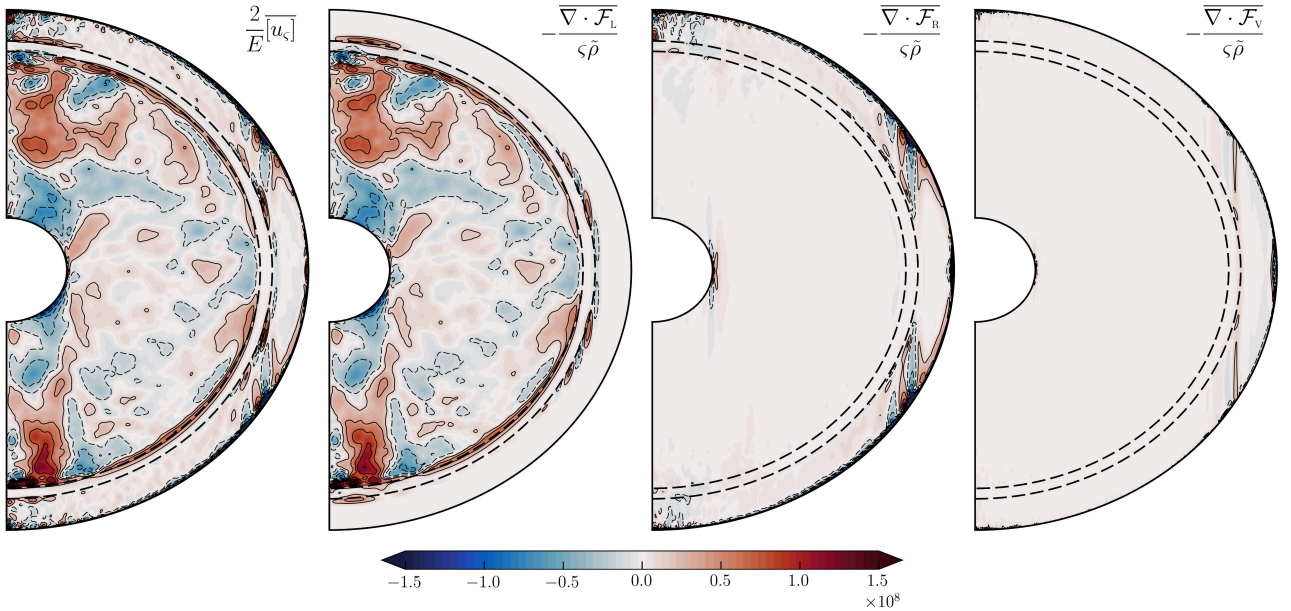


**Figure 13:** Meridional cuts of the time-averaged terms that enter the angular momentum transport equation (35). The dashed half circles mark the bounds of the SSL  $\mathcal{R}_i$  and  $\mathcal{R}_o$ .

To examine the force balance that sustains the meridional circulation pattern, we now consider the zonal component of the Navier-Stokes equation (8):

$$\bar{\rho} \frac{\partial [u_\phi]}{\partial t} + \frac{2}{E} \bar{\rho} [u_\zeta] = -\frac{1}{\zeta} \nabla \cdot \mathbf{F}, \quad (35)$$

where  $u_\zeta$  corresponds to the cylindrically-radial component of the velocity. The angular momentum flux  $\mathbf{F}$  can be decomposed into three contributions,

$$\mathbf{F} = \mathbf{F}_R + \mathbf{F}_M + \mathbf{F}_V,$$

accounting for Reynolds, Maxwell and viscous stresses

$$\mathbf{F}_R = \bar{\rho} \zeta [\mathbf{u} \mathbf{u}_\phi], \quad \mathbf{F}_M = -\frac{\zeta [\mathbf{B} \mathbf{B}_\phi]}{E Pm}, \quad \mathbf{F}_V = -\bar{\rho} \zeta^2 \nabla \left( \frac{[u_\phi]}{\zeta} \right).$$

On time-average, the flow perpendicular to the rotation axis  $[u_\zeta]$  responds to the imbalance between those different axial forces, a physical phenomenon termed “geostrophic pumping” by McIntyre (1998). Figure 13 shows meridional cuts of the different time-averaged contributions to Eq. (35). In the metallic interior, the axisymmetric components of the Lorentz and Coriolis forces balance each other almost

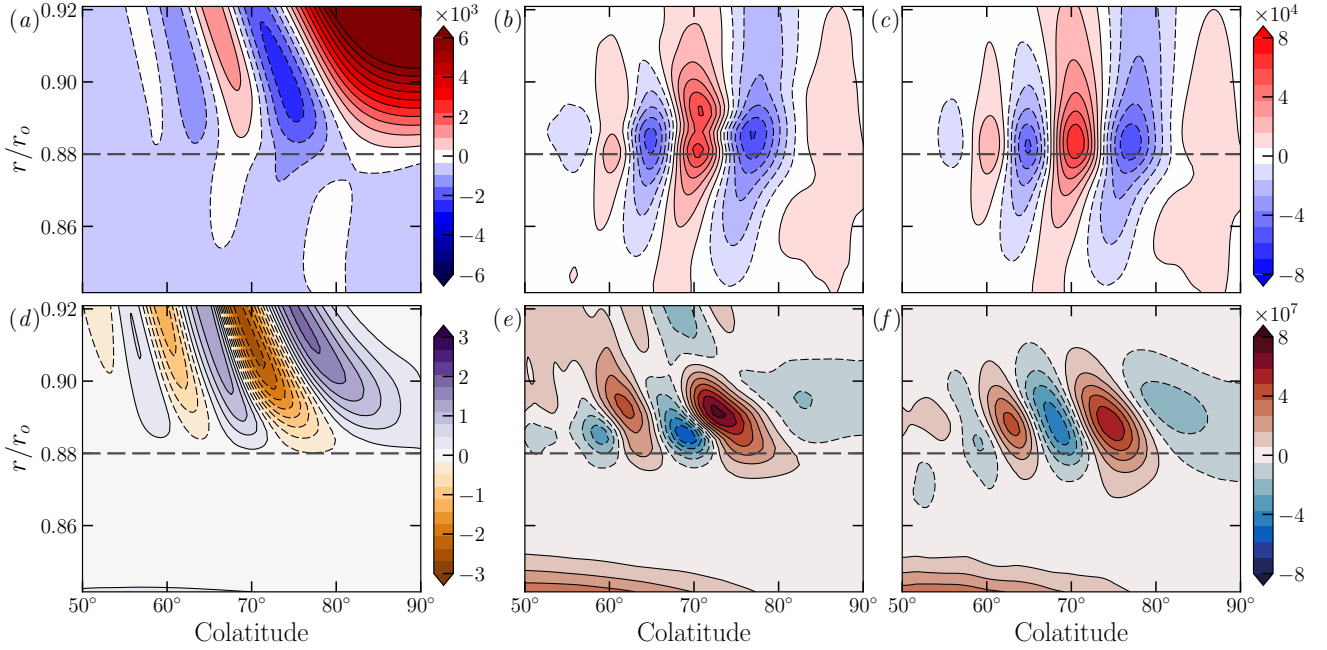


**Figure 14:** Zoomed-in insets of Fig. 11, 12 and 13 for  $r \in [\mathcal{R}_i, 0.92 r_o]$  and  $\theta \in [50^\circ, 90^\circ]$ . (a) Time-averaged zonal flows  $\overline{[u_\phi]}$ . (b) Time-averaged axial gradient of the zonal flows  $2\partial\overline{[u_\phi]}/\partial z$ . (c) Time-averaged meridional gradient of temperature  $(RaE/Pr)(\bar{\alpha}\bar{T}\bar{g}/r)\partial\overline{[s' ]}/\partial\theta$ . (d) Time-averaged stream function of the meridional circulation  $\bar{\Psi}$ . (e) Time-averaged axisymmetric component of Coriolis force  $2\overline{[u_\phi]}/E$ . (f) Time-averaged axisymmetric  $\phi$ -component of the Lorentz force  $-\nabla \cdot \overline{\mathcal{F}_L}/\bar{\rho}_\zeta$ . (b) and (c) correspond to the dominant terms of thermal wind balance (34) shown in Fig. 12. (e) and (f) correspond to the dominant terms of the angular momentum transport equation (35) shown in Fig. 13. In each panel, the horizontal dashed line corresponds to  $r = \mathcal{R}_o$ .

perfectly with secondary contributions of inertia close to the inner boundary. This pattern is typical of rapidly-rotating convection when Lorentz forces play a dominant role in the force balance (see, e.g. Aubert, 2005, his Fig. 7).

The situation in the external convective region (beyond  $\mathcal{R}_o$ ) is more intricate. The Reynolds stresses that maintain the observed alternating zonal jet pattern mainly act in the upper parts of the external convective layer, where the typical convective flows are more vigorous. This driving is compensated partly by viscous stresses in the intense shear regions and partly by Maxwell stresses at the bottom of the external convective region ( $r \gtrsim \mathcal{R}_o$ ) where the electrical conductivity is still sizeable. Maxwell stresses play a negligible role for the equatorial jet since it penetrates less deep. However, they are definitely important for braking the flanking jets.

At the upper edge of the SSL, the delicate balance between Maxwell and Reynolds stresses drives a meridional circulation pattern which slightly penetrates the stable layer. This is the main player in establishing the latitudinal entropy variation that explains the quenching of the zonal winds. Figure 14 illustrates the interesting dynamics in the region where the jets touch the upper edge of the stable layer. The upper row highlights the importance of the thermal wind balance (Eq. 34) for limiting the depth of the flanking jets. The z-variation (panel b) in the zonal flows (panel a) are nearly perfectly explained by the thermal wind term

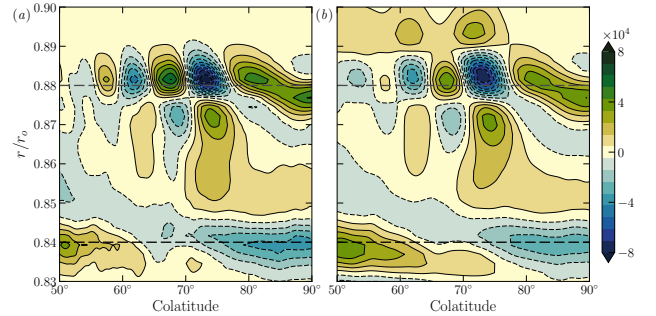


**Figure 15:** Zoomed-in insets for  $r \in [0.83 r_o, 0.9, r_o]$  and  $\theta \in [50^\circ, 90^\circ]$ . (a) Time-averaged axisymmetric advection of the entropy background by the meridional flow  $\bar{\rho}\bar{T}\overline{[u_r]d\bar{s}/dr}$ . (b) Time-averaged radial part of the entropy diffusion  $1/Pr\nabla \cdot (\bar{\rho}\bar{T}\nabla\overline{[s' ]} \cdot \mathbf{e}_r)$ . In both panels the horizontal dashed lines correspond to  $r = \mathcal{R}_i$  and  $r = \mathcal{R}_o$ .

that depends on axisymmetric latitudinal entropy variations (panel c).

The lower row of Fig. 14 illustrates how the stable stratification effectively prevents the meridional circulation (panels d and e) from penetrating the SSL. Azimuthal Lorentz force (panel f) shapes the meridional circulation pattern (panel e) according to Eq. (35). This force is a direct result of the electric currents induced by the zonal winds (Wicht et al., 2019a).

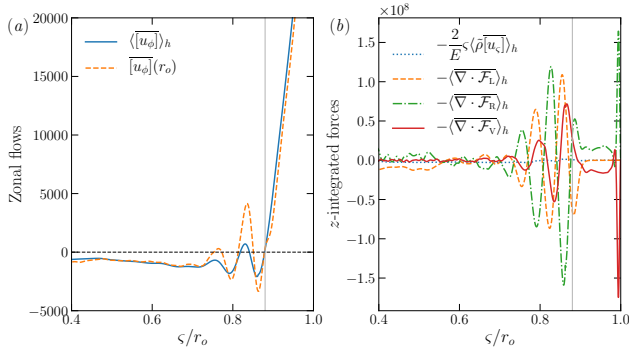


**Figure 16:** (a) Time-averaged surface zonal flows in the Northern hemisphere (dashed lines) and geostrophic zonal flows (solid lines) as a function of the normalised cylindrical radius. (b) Time-averaged axial torques integrated over cylinders as a function of  $\zeta/r_o$ . The vertical lines correspond to the upper edge of the SSL  $\mathcal{R}_o$ .

Figure 15 shows that the time-averaged advection of the entropy background  $d\bar{s}/dr$  by the meridional flow  $\overline{[u_r]}$  is balanced to a large degree by the radial diffusion  $1/Pr \nabla \cdot (\bar{\rho} \bar{T} \nabla [s']) \cdot e_r$ . Other entropy transport contributions are of secondary importance close to the SSL. This implies that the meridional circulation cells which scratch the upper edge of the SSL build up the local latitudinal entropy gradients visible in panel (c) of Fig. 14.

To study the roles played by the Lorentz force and viscosity in controlling the amplitude of the zonal jets, we integrate Eq. (35) over axial cylinders for the fluid regions above the middle of the SSL.

$$\frac{2}{E} s \langle \bar{\rho} [u_s] \rangle_h = - \langle \nabla \cdot \mathcal{F}_R \rangle_h - \langle \nabla \cdot \mathcal{F}_M \rangle_h - \langle \nabla \cdot \mathcal{F}_V \rangle_h. \quad (36)$$

The operator  $\langle f \rangle_h$  is defined by

$$\langle f \rangle_h = \frac{1}{h^+ - h^-} \int_{h^-}^{h^+} f(\zeta, z) dz.$$

where the bounds of integration  $h^+$  and  $h^-$  depend on the radius  $\mathcal{R}_c = \frac{1}{2}(\mathcal{R}_o + \mathcal{R}_i)$ . For  $\zeta \geq \mathcal{R}_c$ ,  $h^\pm = \pm \sqrt{r_o^2 - \zeta^2}$ , while the integration bounds are restricted to the Northern hemisphere for  $\zeta < \mathcal{R}_c$ , i.e.  $h^+ = \sqrt{r_o^2 - \zeta^2}$  and  $h^- = \sqrt{\mathcal{R}_c^2 - \zeta^2}$ .

Figure 16a shows the geostrophic component of the zonal flows,  $\langle [u_\phi] \rangle_h$ , along with the surface profile  $[u_\phi](r_o)$ , while Fig. 16b portrays the different time-averaged axial torques which enter Eq. (36). As already observed in Fig. 11, the upper edge of the SSL marks a clear separation of the zonal flow morphology. For  $\zeta > \mathcal{R}_o$ , the geostrophic component of the zonal flows closely follows the surface profile, indicating the high degree of geostrophy of the main prograde equatorial jet. Because of the decay of the zonal

flows in the SSL, the secondary jets between  $0.7 r_o < \zeta < \mathcal{R}_o$  feature a much weaker geostrophic component. This dynamical change in the vicinity of  $\mathcal{R}_o$  is also recovered in the spatial distribution of the axial torques. The strong prograde equatorial jet is driven by positive Reynolds stresses equilibrated by viscosity, while the geostrophic part of the secondary alternating jets are driven by undulating Reynolds stresses balanced by a combination of Lorentz and viscous torques. The cylindrical integration of the Coriolis term vanishes indicating the cancellation of the mass flux over the considered fluid domain  $r \geq \mathcal{R}_c$ .

## 4. Discussion and conclusion

Several recent Jupiter's interior models suggest that Helium demixing could happen in a thin layer located close to the transition to metallic hydrogen (e.g. Militzer et al., 2016; Wahl et al., 2017; Debras and Chabrier, 2019). To examine the effects of such a layer, we have developed the first global dynamo model of Jupiter that incorporates a stably-stratified layer between  $0.82 R_J$  and  $0.86 R_J$ . The chosen degree of stratification characterised by the ratio of the Brunt-Väisälä frequency to the rotation rate is rather strong with  $N_m/\Omega \simeq 10$  to ensure that convection would not penetrate through the stably-stratified layer (SSL). Such an SSL effectively separates the dynamics of the regions below and above. Previous simulations without such a layer suggest that only the equatorial jet is compatible with Jupiter-like dynamo action (Jones, 2014; Gastine et al., 2014b). Stronger flanking jets would always penetrate into the highly-conducting interior and lead to too complex fields unlike Jupiter (Duarte et al., 2013; Dietrich and Jones, 2018). For the first time, we show that the SSL allows flanking jets to develop while maintaining dipole-dominated dynamo action. The flanking jets only extend up to  $\pm 40^\circ$  degree in latitude and are weaker than observed on Jupiter.

The dynamics below and above the SSL obey different underlying force balances. By directly measuring the spectral distribution of forces, we have shown that the metallic region is controlled by a triple force balance between the non-geostrophic part of Coriolis force, buoyancy and Lorentz forces, with secondary contributions of inertia and viscosity. This forms the so-called *QG-MAC* balance which has been devised by Davidson (2013), and is expected to hold in the dynamo regions of gas giants. The outer convective region where the electrical conductivity drops follows a different force balance with dominant contributions of ageostrophic Coriolis force, buoyancy and inertia. This corresponds to the so-called *QG-IAC* balance (see Cardin and Olson, 1994; Aubert, Gillet and Cardin, 2003; Gillet and Jones, 2006; Gastine et al., 2016), a physical regime at work in convective regions of rapidly-rotating astrophysical bodies when the magnetic effects are negligible. Despite diffusivities orders of magnitudes larger than in the gas giants, the dynamo model presented here obeys the leading order force balances expected to hold in Jupiter's interior.

The mechanism that prevents the jets from penetrating the SSL in our simulations follows the scenario outlined by Christensen et al. (2020). Where the zonal winds reach to high conductivities, their induction yields Lorentz forces that in turn drive a complex meridional circulation pattern. Where this circulation penetrates the SSL and encounters the strong background stratification, the entropy pattern is significantly altered, resulting in a thermal wind balance consistent with the quenching of the winds (e.g. Showman et al., 2006; Augustson, Brown, Brun, Miesch and Toomre, 2012).

Whether the magnetic effects are always required to confine the meridional circulation remains unclear. Indeed, in non-magnetic simulations, viscous and thermal diffusion would mediate the penetration of the zonal winds into the SSL (Spiegel and Zahn, 1992). Given the large diffusivities adopted in global dynamo models, the penetration would be likely much more effective than realistic. In the context of modelling solar-type stars, Brun et al. (2017) developed several non-magnetic numerical models in which the diffusivities are several orders of magnitude smaller in the SSL than in the convective envelope. This yields zonal flows that do not spread into the stably-stratified core (see their Fig. 11), at least on timescales smaller than the thermal diffusion time of the SSL.

The surface field in our simulation is too dipolar and shows too little localised field concentration when compared with the Jupiter field model JRM09 by Connerney et al. (2018). The magnetic spectrum at the bottom of the stable layer at  $0.84 R_J$  is roughly compatible with JRM09 when upward-continued as a potential field. However, the skin effect and to a large degree also the dynamo action just above the stable layer heavily modifies the field, making it less realistic.

The efficiency of the dynamo action above the stable layer depends on the magnetic Reynolds number  $Rm = U_z d_\sigma \sigma \mu_0$  that is based on the zonal flow amplitude  $U_z$  and the electrical conductivity scale height  $d_\sigma = |\partial \ln \sigma / \partial r|^{-1}$  (Liu et al., 2008; Cao and Stevenson, 2017; Wicht et al., 2019a). Observations of the magnetic field variations suggest that this magnetic Reynolds number, which increases with depth, reaches a value around unity at  $0.95 R_J$  (Moore et al., 2019). Gravity measurements indicate that this is also about the depth where the zonal wind velocity decreases rapidly (Kaspi et al., 2018; Galanti and Kaspi, 2021).

Additional support for the upper boundary comes from the fact that the width of the dominant equatorial jet on Jupiter ( $\approx 30^\circ$ ) is only reproduced in numerical models when  $\mathcal{R}_o = 0.95 R_J$  (Gastine et al., 2014a; Heimpel et al., 2016).

Recent interior models by Debras and Chabrier (2019) suggest a stably-stratified layer starting around 0.1 Mbar, which would correspond to a somewhat deeper radius around  $\mathcal{R}_o = 0.93 R_J$ . However, the observational constraints (gravity, He abundance) likely also allow for a shallower layer. Helium demixing, considered as the best candidate to promote stable stratification in Jupiter, is expected where

hydrogen becomes metallic and thus likely significantly deeper around  $0.9 R_J$ . The possible physical origin of a stable layer that would start around  $0.95 R_J$  remains unclear.

The simulation presented here is the first to demonstrate that multiple zonal jets and Jupiter-like dynamo action can be consolidated in a global simulation. The necessary ingredient is a stably-stratified layer that allows zonal jets to develop in the outer envelope without contributing to the dynamo action in the deeper metallic region.

While the simulation presented here is an important step towards more Jupiter-like models, there is certainly room for improvements. The simulation was performed at an Ekman number of  $E = 10^{-6}$  with considerable numerical costs. We speculate that an even smaller Ekman number, and possibly a larger Rayleigh number, is required to drive a stronger jet system that extends to yet higher latitudes. The magnetic field in our simulation could become more Jupiter-like for a stable layer that is thinner and lies closer to the surface than in our simulations. However, this would further increase the numerical costs. The magnetic field also lacks the characteristic banded structure that Gastine et al. (2014b) attributed to zonal wind dynamo action. An increase of the conductivity, or rather the magnetic Reynolds number  $Rm$ , in the outer envelope in our simulation could help here. These open questions pave the way of future global Jovian dynamo models.

## Acknowledgements

We thank Dave Stevenson and an anonymous reviewer for their useful comments. Numerical computations have been carried out on the S-CAPAD platform at IPGP, on the occigen cluster at GENCI-CINES (Grant A0020410095) and on the cobra cluster in Garching. All the figures have been generated using matplotlib (Hunter, 2007) and paraview (<https://www.paraview.org>). The colormaps come from the cmocean package by Thyng, Greene, Hetland, Zimmerle and DiMarco (2016).

## A. Approximations for the background state

To ensure that our numerical models could be computed again by other groups, we approximate the gravity profile  $\tilde{g}$ , the expansion coefficient  $\tilde{\alpha}$  and the Grüneisen parameter  $\tilde{\Gamma}$  by simple interpolations. As shown in Fig. 5, this yields a good agreement with the profile from French et al. (2012).

The dimensionless gravity profile is approximated by the following fourth-order polynomial of the dimensionless radius  $r$

$$\tilde{g}(r) = \sum_{i=0}^4 a_i^g r^i, \quad (37)$$

where  $a^g \simeq [0, 2.435, 0.162, -2.008, 0.665]$ . The expansion coefficient is expressed by the following ninth-order polynomial

$$\ln \tilde{\alpha}(r) = \sum_{i=0}^9 a_i^\alpha r^i, \quad (38)$$

where  $a^\alpha \simeq [1.589, -1.228, 4.532, -0.084, 35.011, 70.455, -27.158, 56.861, 64.873, -19.790]$ .

The interior model of French et al. (2012) suggests rapid variations of the Grüneisen parameter in the outer 15% of Jupiter (see Fig. 3e). It drops from a value of an almost constant value of 0.7 – 0.8 in the metallic core down to 0.2 around  $0.9 R_J$ . To account for this variation, we approximate the radial dependence of the dimensionless Grüneisen parameter by a tanh function

$$\tilde{\Gamma}(r) \simeq 1.313 - 0.392 \tanh [39.2(r - 1.122)]. \quad (39)$$

## References

- Alvan, L., Brun, A.S., Mathis, S., 2014. Theoretical seismology in 3D: nonlinear simulations of internal gravity waves in solar-like stars. *A&A* 565, A42.
- Anufriev, A.P., Jones, C.A., Soward, A.M., 2005. The Boussinesq and anelastic liquid approximations for convection in the Earth's core. *Physics of the Earth and Planetary Interiors* 152, 163–190.
- Aubert, J., 2005. Steady zonal flows in spherical shell dynamos. *Journal of Fluid Mechanics* 542, 53–67.
- Aubert, J., Brito, D., Nataf, H.C., Cardin, P., Masson, J.P., 2001. A systematic experimental study of rapidly rotating spherical convection in water and liquid gallium. *Physics of the Earth and Planetary Interiors* 128, 51–74.
- Aubert, J., Gastine, T., Fournier, A., 2017. Spherical convective dynamos in the rapidly rotating asymptotic regime. *Journal of Fluid Mechanics* 813, 558–593.
- Aubert, J., Gillet, N., Cardin, P., 2003. Quasigeostrophic models of convection in rotating spherical shells. *Geochemistry, Geophysics, Geosystems* 4, 1052.
- Augustson, K.C., Brown, B.P., Brun, A.S., Miesch, M.S., Toomre, J., 2012. Convection and Differential Rotation in F-type Stars. *ApJ* 756, 169.
- Augustson, K.C., Brun, A.S., Toomre, J., 2016. The Magnetic Furnace: Intense Core Dynamos in B Stars. *ApJ* 829, 92.
- Aurnou, J.M., King, E.M., 2017. The cross-over to magnetostrophic convection in planetary dynamo systems. *Proceedings of the Royal Society of London Series A* 473, 20160731.
- Bolton, S.J., Lunine, J., Stevenson, D., Connerney, J.E.P., Levin, S., Owen, T.C., Bagenal, F., Gautier, D., Ingersoll, A.P., Orton, G.S., Guillot, T., Hubbard, W., Bloxham, J., Coradini, A., Stephens, S.K., Mokashi, P., Thorne, R., Thorpe, R., 2017. The Juno Mission. *Space Sci. Rev.* 213, 5–37.
- Braginsky, S.I., Roberts, P.H., 1995. Equations governing convection in earth's core and the geodynamo. *Geophysical and Astrophysical Fluid Dynamics* 79, 1–97.
- Brown, B.P., Vasil, G.M., Zweibel, E.G., 2012. Energy Conservation and Gravity Waves in Sound-proof Treatments of Stellar Interiors. Part I. Anelastic Approximations. *ApJ* 756, 109.
- Browning, M., Brun, A.S., Toomre, J., 2004. Simulations of Core Convection in Rotating A-Type Stars: Differential Rotation and Overshooting. *ApJ* 601, 512–529.
- Brun, A.S., Miesch, M.S., Toomre, J., 2011. Modeling the Dynamical Coupling of Solar Convection with the Radiative Interior. *ApJ* 742, 79.
- Brun, A.S., Strugarek, A., Varela, J., Matt, S.P., Augustson, K.C., Emeriau, C., DoCao, O.L., Brown, B., Toomre, J., 2017. On Differential Rotation and Overshooting in Solar-like Stars. *ApJ* 836, 192.
- Busse, F.H., 1976. A Simple Model of Convection in the Jovian Atmosphere. *Icarus* 29, 255–260.
- Calkins, M.A., 2018. Quasi-geostrophic dynamo theory. *Physics of the Earth and Planetary Interiors* 276, 182–189.
- Cao, H., Stevenson, D.J., 2017. Zonal flow magnetic field interaction in the semi-conducting region of giant planets. *Icarus* 296, 59–72.
- Cardin, P., Olson, P., 1994. Chaotic thermal convection in a rapidly rotating spherical shell: consequences for flow in the outer core. *Physics of the Earth and Planetary Interiors* 82, 235–259.
- Cho, J., Polvani, L.M., 1996. The morphogenesis of bands and zonal winds in the atmospheres on the giant outer planets. *Science* 273, 335–337.
- Christensen, U., Olson, P., Glatzmaier, G.A., 1999. Numerical modelling of the geodynamo: a systematic parameter study. *Geophysical Journal International* 138, 393–409.
- Christensen, U.R., 2002. Zonal flow driven by strongly supercritical convection in rotating spherical shells. *Journal of Fluid Mechanics* 470, 115–133.
- Christensen, U.R., 2006. A deep dynamo generating Mercury's magnetic field. *Nature* 444, 1056–1058.
- Christensen, U.R., Aubert, J., 2006. Scaling properties of convection-driven dynamos in rotating spherical shells and application to planetary magnetic fields. *Geophysical Journal International* 166, 97–114.
- Christensen, U.R., Wicht, J., 2015. 8.10 - Numerical Dynamo Simulations, in: Schubert, G. (Ed.), *Treatise on Geophysics (Second Edition)*. Elsevier, Oxford, Second edition edition. pp. 245 – 277.
- Christensen, U.R., Wicht, J., Dietrich, W., 2020. Mechanisms for Limiting the Depth of Zonal Winds in the Gas Giant Planets. *ApJ* 890, 61.
- Connerney, J.E.P., Kotsiaros, S., Oliverson, R.J., Espley, J.R., Joergensen, J.L., Joergensen, P.S., Merayo, J.M.G., Hecceg, M., Bloxham, J., Moore, K.M., Bolton, S.J., Levin, S.M., 2018. A New Model of Jupiter's Magnetic Field From Juno's First Nine Orbits. *Geophys. Res. Lett.* 45, 2590–2596.
- Davidson, P.A., 2013. Scaling laws for planetary dynamos. *Geophysical Journal International* 195, 67–74.
- Debras, F., Chabrier, G., 2019. New Models of Jupiter in the Context of Juno and Galileo. *ApJ* 872, 100.
- Dietrich, W., Jones, C.A., 2018. Anelastic spherical dynamos with radially variable electrical conductivity. *Icarus* 305, 15–32.
- Dietrich, W., Wicht, J., 2018. Penetrative Convection in Partly Stratified Rapidly Rotating Spherical Shells. *Frontiers in Earth Science* 6, 189.
- Duarte, L.D.V., Gastine, T., Wicht, J., 2013. Anelastic dynamo models with variable electrical conductivity: An application to gas giants. *Physics of the Earth and Planetary Interiors* 222, 22–34.
- Duarte, L.D.V., Wicht, J., Gastine, T., 2018. Physical conditions for Jupiter-like dynamo models. *Icarus* 299, 206–221.
- Elstner, D., Meinel, R., Rüdiger, G., 1990. Galactic dynamo models without sharp boundaries. *Geophysical and Astrophysical Fluid Dynamics* 50, 85–94.
- French, M., Becker, A., Lorenzen, W., Nettelmann, N., Bethkenhagen, M., Wicht, J., Redmer, R., 2012. Ab Initio Simulations for Material Properties along the Jupiter Adiabatic. *ApJS* 202, 5.
- Galanti, E., Kaspi, Y., 2021. Combined magnetic and gravity measurements probe the deep zonal flows of the gas giants. *MNRAS* 501, 2352–2362.
- Gastine, T., Aubert, J., Fournier, A., 2020. Dynamo-based limit to the extent of a stable layer atop Earth's core. *Geophysical Journal International* 222, 1433–1448.
- Gastine, T., Heimpel, M., Wicht, J., 2014a. Zonal flow scaling in rapidly-rotating compressible convection. *Physics of the Earth and Planetary Interiors* 232, 36–50.
- Gastine, T., Wicht, J., 2012. Effects of compressibility on driving zonal flow in gas giants. *Icarus* 219, 428–442.
- Gastine, T., Wicht, J., Aubert, J., 2016. Scaling regimes in spherical shell rotating convection. *Journal of Fluid Mechanics* 808, 690–732.
- Gastine, T., Wicht, J., Duarte, L.D.V., Heimpel, M., Becker, A., 2014b. Explaining Jupiter's magnetic field and equatorial jet dynamics. *Geophys. Res. Lett.* 41, 5410–5419.
- Gillet, N., Jones, C.A., 2006. The quasi-geostrophic model for rapidly rotating spherical convection outside the tangent cylinder. *Journal of*

- Fluid Mechanics 554, 343–369.
- Gilman, P.A., Glatzmaier, G.A., 1981. Compressible convection in a rotating spherical shell - I - Anelastic equations. *ApJS* 45, 335–349.
- Glatzmaier, G.A., 1984. Numerical simulations of stellar convective dynamos. I - The model and method. *Journal of Computational Physics* 55, 461–484.
- Gómez-Pérez, N., Heimpel, M., Wicht, J., 2010. Effects of a radially varying electrical conductivity on 3D numerical dynamos. *Physics of the Earth and Planetary Interiors* 181, 42–53.
- Gough, D.O., 1969. The Anelastic Approximation for Thermal Convection. *Journal of Atmospheric Sciences* 26, 448–456.
- Heimpel, M., Aurnou, J., 2007. Turbulent convection in rapidly rotating spherical shells: A model for equatorial and high latitude jets on Jupiter and Saturn. *Icarus* 187, 540–557.
- Heimpel, M., Aurnou, J., Wicht, J., 2005. Simulation of equatorial and high-latitude jets on Jupiter in a deep convection model. *Nature* 438, 193–196.
- Heimpel, M., Gastine, T., Wicht, J., 2016. Simulation of deep-seated zonal jets and shallow vortices in gas giant atmospheres. *Nature Geoscience* 9, 19–23.
- Heimpel, M., Gómez Pérez, N., 2011. On the relationship between zonal jets and dynamo action in giant planets. *Geophys. Res. Lett.* 38, L14201.
- Hunter, J.D., 2007. Matplotlib: A 2d graphics environment. *Computing In Science & Engineering* 9, 90–95.
- Iess, L., Folkner, W.M., Durante, D., Parisi, M., Kaspi, Y., Galanti, E., Guillot, T., Hubbard, W.B., Stevenson, D.J., Anderson, J.D., Buccino, D.R., Casajus, L.G., Milani, A., Park, R., Racioppa, P., Serra, D., Tortora, P., Zannoni, M., Cao, H., Helled, R., Lunine, J.I., Miguel, Y., Militzer, B., Wahl, S., Connerney, J.E.P., Levin, S.M., Bolton, S.J., 2018. Measurement of Jupiter’s asymmetric gravity field. *Nature* 555, 220–222.
- Jones, C.A., 2014. A dynamo model of Jupiter’s magnetic field. *Icarus* 241, 148–159.
- Jones, C.A., 2015. 8.05 Thermal and Compositional Convection in the Outer Core, in: Schubert, G. (Ed.), *Treatise on Geophysics* (Second Edition). Elsevier, Oxford, Second edition edition. pp. 115–159.
- Jones, C.A., Boronski, P., Brun, A.S., Glatzmaier, G.A., Gastine, T., Miesch, M.S., Wicht, J., 2011. Anelastic convection-driven dynamo benchmarks. *Icarus* 216, 120–135.
- Jones, C.A., Kuzanyan, K.M., 2009. Compressible convection in the deep atmospheres of giant planets. *Icarus* 204, 227–238.
- Julien, K., Knobloch, E., Rubio, A.M., Vasil, G.M., 2012. Heat Transport in Low-Rossby-Number Rayleigh-Bénard Convection. *Phys. Rev. Lett.* 109, 254503.
- Kaspi, Y., Galanti, E., Hubbard, W.B., Stevenson, D.J., Bolton, S.J., Iess, L., Guillot, T., Bloxham, J., Connerney, J.E.P., Cao, H., Durante, D., Folkner, W.M., Helled, R., Ingersoll, A.P., Levin, S.M., Lunine, J.I., Miguel, Y., Militzer, B., Parisi, M., Wahl, S.M., 2018. Jupiter’s atmospheric jet streams extend thousands of kilometres deep. *Nature* 555, 223–226.
- King, E.M., Stellmach, S., Aurnou, J.M., 2012. Heat transfer by rapidly rotating Rayleigh-Bénard convection. *Journal of Fluid Mechanics* 691, 568–582.
- Knudson, M.D., Desjarlais, M.P., Preising, M., Redmer, R., 2018. Evaluation of exchange-correlation functionals with multiple-shock conductivity measurements in hydrogen and deuterium at the molecular-to-atomic transition. *Phys. Rev. B* 98, 174110.
- Kong, D., Zhang, K., Schubert, G., Anderson, John, D., 2018. Origin of Jupiter’s cloud-level zonal winds remains a puzzle even after Juno. *Proceedings of the National Academy of Science* 115, 8499–8504.
- Kosloff, D., Tal-Ezer, H., 1993. A Modified Chebyshev Pseudospectral Method with an  $O(N^{-1})$  Time Step Restriction. *Journal of Computational Physics* 104, 457–469.
- Kuang, W., Bloxham, J., 1999. Numerical Modeling of Magnetohydrodynamic Convection in a Rapidly Rotating Spherical Shell: Weak and Strong Field Dynamo Action. *Journal of Computational Physics* 153, 51–81.
- Lantz, S.R., Fan, Y., 1999. Anelastic magnetohydrodynamic equations for modeling solar and stellar convection zones. *ApJS* 121, 247–264.
- Lecoanet, D., Brown, B.P., Zweibel, E.G., Burns, K.J., Oishi, J.S., Vasil, G.M., 2014. Conduction in Low Mach Number Flows. I. Linear and Weakly Nonlinear Regimes. *ApJ* 797, 94.
- Lian, Y., Showman, A.P., 2010. Generation of equatorial jets by large-scale latent heating on the giant planets. *Icarus* 207, 373–393.
- Liu, J., Goldreich, P.M., Stevenson, D.J., 2008. Constraints on deep-seated zonal winds inside Jupiter and Saturn. *Icarus* 196, 653–664.
- Lorenzen, W., Holst, B., Redmer, R., 2011. Metallization in hydrogen-helium mixtures. *Phys. Rev. B* 84, 235109.
- McIntyre, M.E., 1998. Breaking Waves and Global-Scale Chemical Transport in the Earth’s Atmosphere, with Spinoffs for the Sun’s Interior. *Progress of Theoretical Physics Supplement* 130, 137–166.
- Militzer, B., Soubiran, F., Wahl, S.M., Hubbard, W., 2016. Understanding Jupiter’s Interior. *J. Geophys. Res.* 121, 1152–1172.
- Moore, K.M., Cao, H., Bloxham, J., Stevenson, D.J., Connerney, J.E.P., Bolton, S.J., 2019. Time variation of Jupiter’s internal magnetic field consistent with zonal wind advection. *Nature Astronomy* 3, 730–735.
- Moore, K.M., Yadav, R.K., Kulowski, L., Cao, H., Bloxham, J., Connerney, J.E.P., Kotsiaros, S., Jørgensen, J.L., Merayo, J.M.G., Stevenson, D.J., Bolton, S.J., Levin, S.M., 2018. A complex dynamo inferred from the hemispheric dichotomy of Jupiter’s magnetic field. *Nature* 561, 76–78.
- Nellis, W.J., Weir, S.T., Mitchell, A.C., 1999. Minimum metallic conductivity of fluid hydrogen at 140 GPa (1.4 Mbar). *Phys. Rev. B* 59, 3434–3449.
- Rhines, P.B., 1975. Waves and turbulence on a beta-plane. *Journal of Fluid Mechanics* 69, 417–443.
- Ridley, V.A., Holme, R., 2016. Modeling the Jovian magnetic field and its secular variation using all available magnetic field observations. *Journal of Geophysical Research (Planets)* 121, 309–337.
- Schaeffer, N., 2013. Efficient spherical harmonic transforms aimed at pseudospectral numerical simulations. *Geochemistry, Geophysics, Geosystems* 14, 751–758.
- Schöttler, M., Redmer, R., 2018. Ab Initio Calculation of the Miscibility Diagram for Hydrogen-Helium Mixtures. *Phys. Rev. Lett.* 120, 115703.
- Schwaiger, T., Gastine, T., Aubert, J., 2019. Force balance in numerical geodynamo simulations: a systematic study. *Geophysical Journal International*, 197.
- Schwaiger, T., Gastine, T., Aubert, J., 2021. Relating force balances and flow length scales in geodynamo simulations. *Geophysical Journal International* 224, 1890–1904.
- Showman, A.P., Gierasch, P.J., Lian, Y., 2006. Deep zonal winds can result from shallow driving in a giant-planet atmosphere. *Icarus* 182, 513–526.
- Spiegel, E.A., Zahn, J.P., 1992. The solar tachocline. *A&A* 265, 106–114.
- Stevenson, D.J., 1980. Saturn’s luminosity and magnetism. *Science* 208, 746–748.
- Stevenson, D.J., 2020. Jupiter’s Interior as Revealed by Juno. *Annual Review of Earth and Planetary Sciences* 48, 465–489.
- Takehiro, S.I., Lister, J.R., 2001. Penetration of columnar convection into an outer stably stratified layer in rapidly rotating spherical fluid shells. *Earth and Planetary Science Letters* 187, 357–366.
- Takehiro, S.I., Sasaki, Y., 2018. On destruction of a thermally stable layer by compositional convection in the Earth’s outer core. *Frontiers in Earth Science* 6, 192.
- Thyng, K.M., Greene, C.A., Hetland, R.D., Zimmerle, H.M., DiMarco, S.F., 2016. True Colors of Oceanography: Guidelines for Effective and Accurate Colormap Selection. *Oceanography* 29, 10.
- Tilgner, A., 1999. Spectral methods for the simulation of incompressible flows in spherical shells. *International Journal for Numerical Methods in Fluids* 30, 713–724.
- Tsang, Y.K., Jones, C.A., 2020. Characterising Jupiter’s dynamo radius using its magnetic energy spectrum. *Earth and Planetary Science Letters* 530, 115879.
- Vasavada, A.R., Showman, A.P., 2005. Jovian atmospheric dynamics: an update after Galileo and Cassini. *Reports on Progress in Physics* 68, 1935–1996.

- Verhoeven, J., Wiesehöfer, T., Stellmach, S., 2015. Anelastic versus Fully Compressible Turbulent Rayleigh-Bénard Convection. *ApJ* 805, 62.
- Wahl, S.M., Hubbard, W.B., Militzer, B., Guillot, T., Miguel, Y., Movshovitz, N., Kaspi, Y., Helled, R., Reese, D., Galanti, E., Levin, S., Connerney, J.E., Bolton, S.J., 2017. Comparing Jupiter interior structure models to Juno gravity measurements and the role of a dilute core. *Geophys. Res. Lett.* 44, 4649–4659.
- Weir, S.T., Mitchell, A.C., Nellis, W.J., 1996. Metallization of Fluid Molecular Hydrogen at 140 GPa (1.4 Mbar). *Phys. Rev. Lett.* 76, 1860–1863.
- Wicht, J., 2002. Inner-core conductivity in numerical dynamo simulations. *Physics of the Earth and Planetary Interiors* 132, 281–302.
- Wicht, J., Dietrich, W., Wulff, P., Christensen, U.R., 2020. Linking zonal winds and gravity: the relative importance of dynamic self-gravity. *MNRAS* 492, 3364–3374.
- Wicht, J., Gastine, T., Duarte, L.D.V., 2019a. Dynamo Action in the Steeply Decaying Conductivity Region of Jupiter-Like Dynamo Models. *Journal of Geophysical Research (Planets)* 124, 837–863.
- Wicht, J., Gastine, T., Duarte, L.D.V., Dietrich, W., 2019b. Dynamo action of the zonal winds in Jupiter. *A&A* 629, A125.
- Yadav, R.K., Gastine, T., Christensen, U.R., Duarte, L.D.V., 2013. Consistent Scaling Laws in Anelastic Spherical Shell Dynamos. *ApJ* 774, 6.
- Yadav, R.K., Gastine, T., Christensen, U.R., Wolk, S.J., Poppenhaeger, K., 2016. Approaching a realistic force balance in geodynamo simulations. *Proceedings of the National Academy of Science* 113, 12065–12070.